Research Article

Amin Allah Kamali*, Mohsen Moayyed, Nasir Amel, Fadaeian Mohammad, Marco Brenna, Benoit M. Saumur, and José Francisco Santos

Mineralogy, mineral chemistry and thermobarometry of post-mineralization dykes of the Sungun Cu–Mo porphyry deposit (Northwest Iran)

https://doi.org/10.1515/geo-2020-0009
received November 26, 2018; accepted August 13, 2019

Abstract: The Sungun copper–molybdenum porphyry deposit is located in the north of Varzaghan, northwestern Iran. The Sungun quartz-monzonite is the oldest mineralized intrusive body in the region and was emplaced during the Early Miocene. Eight categories of the late and unmineralized dykes, which include quartz diorite, gabbrodiorite, diorite, dacite, microdiorite and lamprophyre (LAM), intrude the ore deposit. The main mineral phases in the dykes include plagioclase, amphibole and biotite, with minor quartz and apatite and secondary chlorite, epidote, muscovite and sericite. The composition of plagioclase in the quartz diorite dykes (DK1a, DK1b and DK1c) varies from albite-oligoclase to andesine and oligoclase to andesine; in the diorite, it varies from andesine to labradorite; in the LAM, from albite to oligoclase; and in the microdiorite (MDI), it occurs as albite. Amphibole compositions are consistent with classification as hornblende or calcic amphibole. Based on their Al^{IV} value (less than 1.5), amphibole compositions are consistent with an active continental margin affinity. The average percentage of pistacite (P_s) in epidotes formed from alteration of plagioclase and ferromagnesian minerals is 27–23% and 25–30%, respectively. Thermobarometric studies based on amphibole and biotite indicate approximate dyke crystallization temperature of 850–750°C, pressure of 231–336 MPa and high fO_2 (>nickel-nickel-oxide buffer). The range of mineral compositions in the postmineralization dyke suite is consistent with a genetic relationship with the subduction of the Neotethys oceanic crust beneath the continental crust of the northwest part of the Central Iranian Structural Zone. Despite the change from calc-alkaline to alkaline magmatism, the dykes are likely related to the late stages of magmatic activity in the subduction system that also generated the porphyry deposit.

Keyword: mineralogy, mineral chemistry, post-mineralization dykes, porphyry deposit, Sungun

1 Introduction

The Arasbaran porphyry copper belt is located in the northwest of Iran and connects the eastern and western parts of the Alps-Himalayan mineralization belt. This belt extends from northwestern Iran to the Garabagh mountains of Azerbaijan and eventually to Armenia and Turkey. The Arasbaran belt is 70 to 80 km wide and 400 km long and includes the Cretaceous and Cenozoic sedimentary and volcanic rocks, as well as the Cenozoic intrusive rocks. Extensive intrusive bodies with different lithologies and age have been emplaced during the Oligocene and the Miocene in the Arasbaran belt [1,2]. In this belt, there are more than 10 areas that host porphyry copper mineralization, among which the Sungun deposit is a world class reserve [3]. The copper and molybdenum mineralization at the Sungun is related to the emplacement of a quartz-monzonite porphyry (the Sungun porphyry) during the Early Miocene. The same area has been affected by subsequent unmineralized intrusive activity that has formed distinct dyke suites, classified on the basis of their lithology, degree of alteration and relative age of emplacement: (i) quartz diorite (DK1a, DK1b and DK1c), (ii) gabbrodiorite (DK2), (iii) diorite

* **Corresponding author: Amin Allah Kamali,** Department of Earth Sciences, Faculty of Natural Sciences, University of Tabriz, Tabriz, 5166616471, Iran, e-mail: aminkamali1984@gmail.com
Mohsen Moayyed, Nasir Amel: Department of Earth Sciences, Faculty of Natural Sciences, University of Tabriz, Tabriz, 5166616471, Iran
Fadaeian Mohammad: Department of Geology, Payame Noor University, Tehran, Iran
Marco Brenna: Department of Geology, University of Otago, Dunedin, 9016, New Zealand
Benoit M. Saumur: Département des Sciences de la Terre et de l'Atmosphère, Université du Québec à Montréal, 201 avenue du Président-Kennedy, Case postale 8888, Succursale Centreville, Montréal, QC, H3C 3P8, Canada
José Francisco Santos: Geobiotec, Department of Geosciences, University of Aveiro, Aveiro, 3810-193, Portugal

(DK3), (iv) dacite (DK4), (v) microdiorite (MDI) and (vi) lamprophyre (LAM) [3]. All dykes generally strike north-west to south-east and dip to the south-west and have undergone moderate to extensive alteration.

Considerable research has been done on the copper–molybdenum hosting porphyry and the associated sulphide mineralization [5–8], but there is relatively little information on the petrographic and mineralogical characteristics of post-mineralization dykes and their significance in terms of the magmatic system within which mineralization formed. The compositions of minerals provide a means of evaluating the physicochemical conditions of magma during the emplacement of the post-mineralization dykes. Here, we present and describe the petrological properties of the post-mineralization dykes at the Sungun, with the aim of determining pressure and temperature of crystallization and interpret their petrogenetic history within the context of regional tectonism and their affinity with the Sungun porphyry.

2 Geology

The Cenozoic Ahar–Arasbaran volcanic belt in northern Iran is part of the Alborz–Azerbaijan magmatic zone, which developed along the southern margin of Eurasia. The volcanic and plutonic rocks have medium- to high-K calc-alkaline to alkaline compositions and show similar geochemical features, indicating a common subduction-metasomatized continental lithospheric mantle source. Granodioritic, tonalitic and quartz-monzonitic plutons provided the heat flux and magmatic fluids that played a major role in the precipitation of porphyry, skarn and epithermal copper, molybdenum and gold deposits [8] (Figure 1).

The Sungun copper deposit is 32 km north of the city of Varzeghan, located in the East Azerbaijan province (Figure 2). The oldest country rock unit in the area consists of thin to medium layers of limestone and shale [9]. Fossils in the limestone constrain its age to the Upper Cretaceous (Campanian–Maastrichtian). These sedimentary units are intruded by a porphyritic quartz-monzonite body (the Sungun porphyry, Figure 3a). The sedimentary beds dip 25°–30° towards the Sungun porphyry to the east, possibly as a result of fault activity along the modern Sungunchay River or the intrusion of unexposed intrusive bodies. The quartz-monzonite intrusion is the oldest igneous body occurring at the Sungun mine, and it hosts Cu–Mo mineralization of the Oligo-Miocene age. The main Sungun porphyritic intrusion crystallized at 20.69 ± 0.37 (±0.2σ) Ma [10]. Skarn occurs at the contact between the Sungun porphyry and the Cretaceous limestone in parts of the northern and eastern mining areas (Figure 3d and e). Skarnification occurs in broad and dispersed lensoidal portions of the mineralized zone. Hornfels is abundant within the carbonate units at the eastern margins of the skarn bodies. There are four alteration zones, including potassic, phyllic and propylitic, in the Sungun porphyry body. The magma feeding the Sungun porphyry evolved in response to magmatic differentiation, fractional crystallization, assimilation and crustal contamination [6].

After the emplacement of the quartz-monzonite, numerous dykes were injected within both the porphyry unit and the older carbonate country rock. These dykes are divided into eight categories based on timing of injection. The first generation of dykes are diorite to quartz diorite (DK1), which are the most abundant post-mineralization intrusions in the Sungun area. Field studies and observations from drill core indicate that DK1 dykes can be further categorized based on their age and type of alteration into three subcategories: DK1a, DK1b and DK1c [11] (Table 1). Within the open pit mine, only DK1a and DK1b dykes are exposed. DK1a dykes were injected at the contact with the limestones, causing weak skarnification in the northern parts of the area (Figure 3b). Zircon U-Pb dating of DK1a and DK1b dykes gives intrusive ages of 20.57 ± 0.45 [10] and 19.85 ± 0.33 Ma [12]. DK1b dykes contain MDI and quartz dioritic enclaves [13] (Figure 3c). DK1b dykes crosscut DK1a dykes. DK1c dykes are exposed in the Eastern skarn zone of the mine area and crosscut both DK1a and DK1b dykes (Figure 3d). The gabbrodiorite dykes (DK2) occur inside the Sungun open pit mine as well as on its northeastern side. The dioritic dykes (DK3) were intruded within the Sungun porphyry and crosscut the DK1 dykes (Figure 3e). The MDI dykes appear in boreholes (Figure 4a) and they cut the quartz dioritic dykes (DK1a and DK1b) [17]. The LAM dykes are not reported in the area, but they appear in boreholes (Figure 4b) [18]. Dacitic to rhyodacitic (DK4) subvolcanic intrusions/cryptodomes of the Pliocene [11] Chaldaqi suite were injected into the Sungun porphyry, and the branching dykes are exposed in various parts of the latter. Dacitic to rhyodacitic dykes (DK4) are the result of the injected branches of the subvolcanic Chaldaqi intrusive bodies into the Sungun porphyry and have the Plio-Quaternary age [11]. These are, however, poorly exposed because they are covered by epithermal, clastic and pyroclastic deposits derived from eruptions of nearby Mount Dashdibi volcano [11].

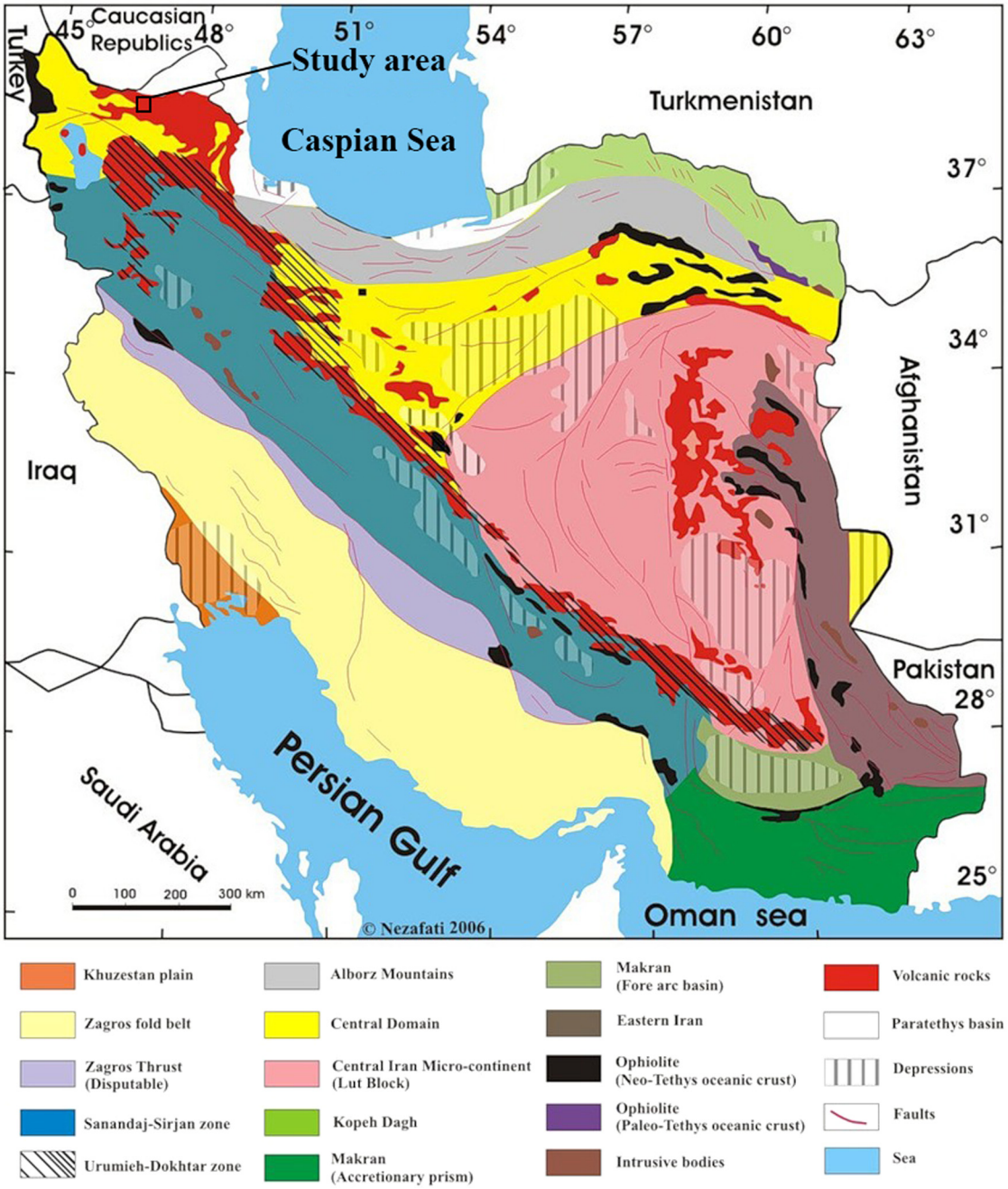

Figure 1: Major geological subdivisions of Iran after [14] and [15], modified after [16], duplicated with permission.

3 Methods

Petrographic studies were performed on 100 samples using polarizing microscopy. Silicate mineral chemistry was performed on plagioclase, amphibole, biotite, chlorite, muscovite and epidote from 12 samples of quartz diorite, diorite, LAM and MDI dykes. Analyses were done in the laboratory of the Iran Mineral Research and Processing Center and using a CAMECA SX100 at the Microprobe Laboratory at the University of Oklahoma, USA, with standard analytical conditions of 20 kV, 20 nA and a 2 mm spot size.

3.1 Petrography

3.1.1 Sungun porphyry quartz-monzonite

The main mineral association in the Sungun porphyry deposit consists of plagioclase (40–45%), orthoclase

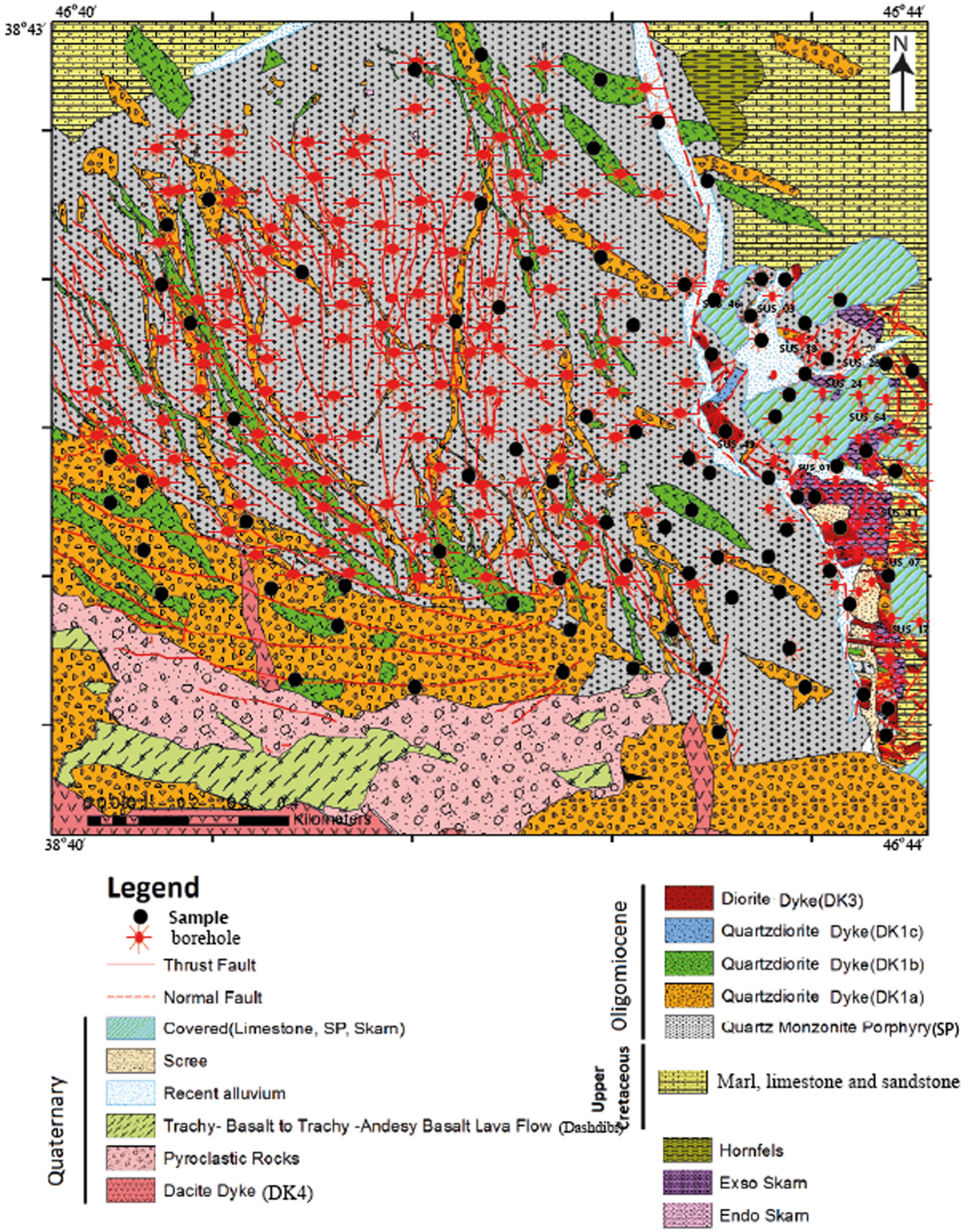

Figure 2: Geological map of the Sungun Copper Mine.

(30–35%), amphibole (5–10%), biotite (5–10%) and quartz (5–10%). Plagioclase is altered to sericite–calcite–epidote in the propylitic zone and entirely decomposed to sericite in the phyllic zone. This mineral is fresh in the potassic zone and rarely altered to sericite. Metasomatic biotite is also observed in the potassic zone. Ferromagnesian minerals such as amphibole and biotite are altered to sericite–calcite–chlorite–epidote associations in the propylitic zone and

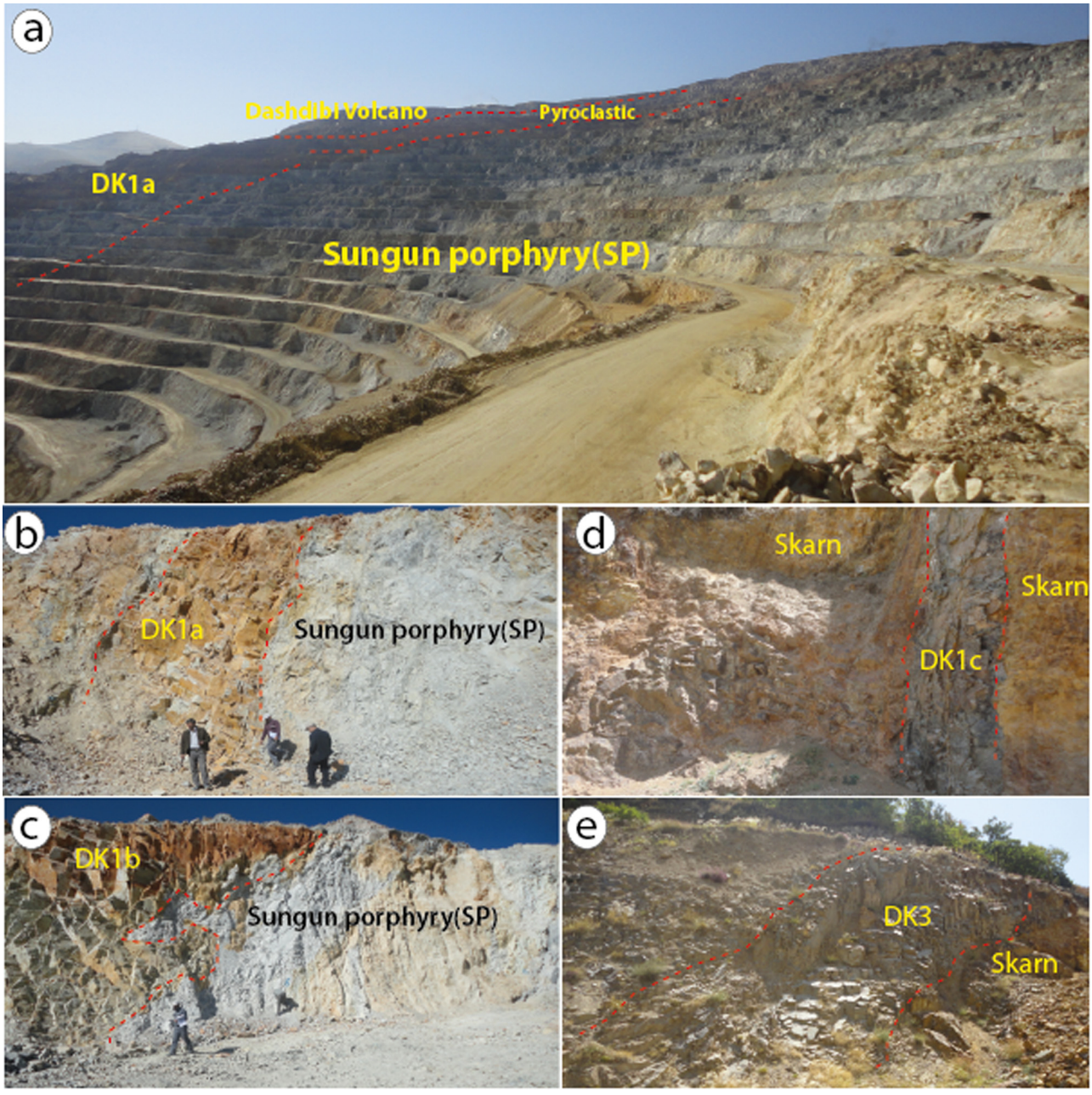

Figure 3: (a) Inside view of the open pit mine of the Sungun porphyry and quartz diorite dyke (DK1a), overlying pyroclastic sediments and deposits of the Mount Dashdibi volcano. (b) Sungun porphyry intruded by the quartz diorite dyke (DK1a). (c) Irregular contact of the DK1b dyke with the Sungun porphyry. (d) Quartz diorite dyke (DK1c) in the eastern skarn zone of the Sungun copper mine. (e) Dioritic dyke (DK3) intruding the Sungun skarn.

entirely replaced by sericite and opaque minerals and negligible chlorite and epidote. Amphibole in the Sungun porphyry is classified as edenite [4].

3.1.2 Quartz diorite dyke: DK1

The quartz diorite dykes are the most abundant intrusive bodies crosscutting the Sungun porphyry. Field studies and drill cores show that three different types of these dykes have been injected into the Sungun porphyry mass; these are therefore divided into three categories DK1b, DK1a and DK1c, according to the age and type of alteration [11].

3.1.3 Quartz diorite dyke: DK1a

The colours of these dykes are bright to light green in hand sample, and they have moderate to severe

Table 1: Summary of characteristics of the post-mineralization dykes observed at the Sungun area

Magma Pulse	Name	Lithology	Field/core observations	Associated alteration	Age	Comments	Ref.
1	DK1a	Quartz diorite	Field	Phyllic	19.8–20.60 Ma		[10–12,51]
1	DK1b	Quartz diorite	Field	Phyllic (L-M), propylitic		Two enclaves: quartz diorite and MDI	[10,51]
1	DK1c	Quartz diorite	Field	Propylitic		Cuts DK1a and DK1b	[10,51]
1	DK3	Diorite	Field	Phyllic (L), propylitic		Two enclaves: diorite and hornfels, cuts DK1a, DK1b and DK1c. Xencryst pyroxene	[10,51]
2	DK2	Gabbrodiorite	Field	Propylitic			[10,51]
3	MDI (DK5)	Microdiorite	Drill core	Phyllic (M)		Borehole (SUS_01,03,07,17,41,43,44,46,52)	[51]
4	LAM (DK6)	Lamprophyre	Drill core	Phyllic (L), propylitic		Borehole (SUS_24,26,38,42,64)	[51]
5	DK4	Dacite/rhyodacite	Field	Propylitic	Plio-Quaternary		[11]

phyllic alteration. They are generally not associated with sulphide mineralization (Figure 5a). The main minerals of this group are plagioclase (50–60%), biotite (15–20%) and amphibole (5–10%). Plagioclase is present as both phenocrysts (0.7–2 mm) and microlites (Figure 6a). Biotite crystals are generally euhedral, but they are often altered to muscovite, calcite, chlorite and sericite (Figure 6a). Amphibole forms subhedral fine-grained (0.5 mm) crystals. The minor mineral phases in these dykes include orthoclase, quartz and apatite (Figure 6a). Texturally, these dykes are porphyritic within a microlytic groundmass.

3.1.4 Quartz diorite dyke: DK1b

DK1b dykes appear greenish to olive green in outcrop and hand sample and were emplaced subsequently to DK1a. They have a very weak phyllic alteration grading to a moderately strong propylitic alteration (Figure 5b) with rare pyrite and no observed mineralization. The main minerals are plagioclase (50–60%), amphibole (20–30%) and biotite (5–10%). Both plagioclase and amphibole crystals are euhedral to subhedral. Amphibole exhibits distinct simple twinning, and in some cases, it is completely altered to chlorite, sericite and epidote (Figure 6b). Biotite is weakly to strongly altered, and in some cases, it is completely replaced by chlorite and sericite and rare muscovite. The minor mineral phases include sphene, apatite and quartz. The overall texture of these dykes is porphyritic within a microlytic groundmass.

3.1.5 Quartz diorite dyke: DK1c

DK1c dykes are dark green in hand specimen and are porphyritic with a fine to medium (1 mm) microlytic groundmass. These dykes are lithologically similar to DK1b and differ only in terms of the intensity of alteration. The main minerals of this rock group include plagioclase (30–40%), biotite (20–30%) and amphibole (15–20%). The phenocrysts of the plagioclase are white and mostly fresh with only very weak propylitic alteration to minor calcite alteration (Figure 5c). Plagioclase forms both subhedral phenocrysts and microlites with polysynthetic twin and oscillatory zoning (Figure 6c). Amphibole crystals are euhedral to subhedral and exhibit twinning (Figure 6c). Biotite in this rock is euhedral to subhedral (Figure 6c). The minor mineral phases include orthoclase, quartz and sphene.

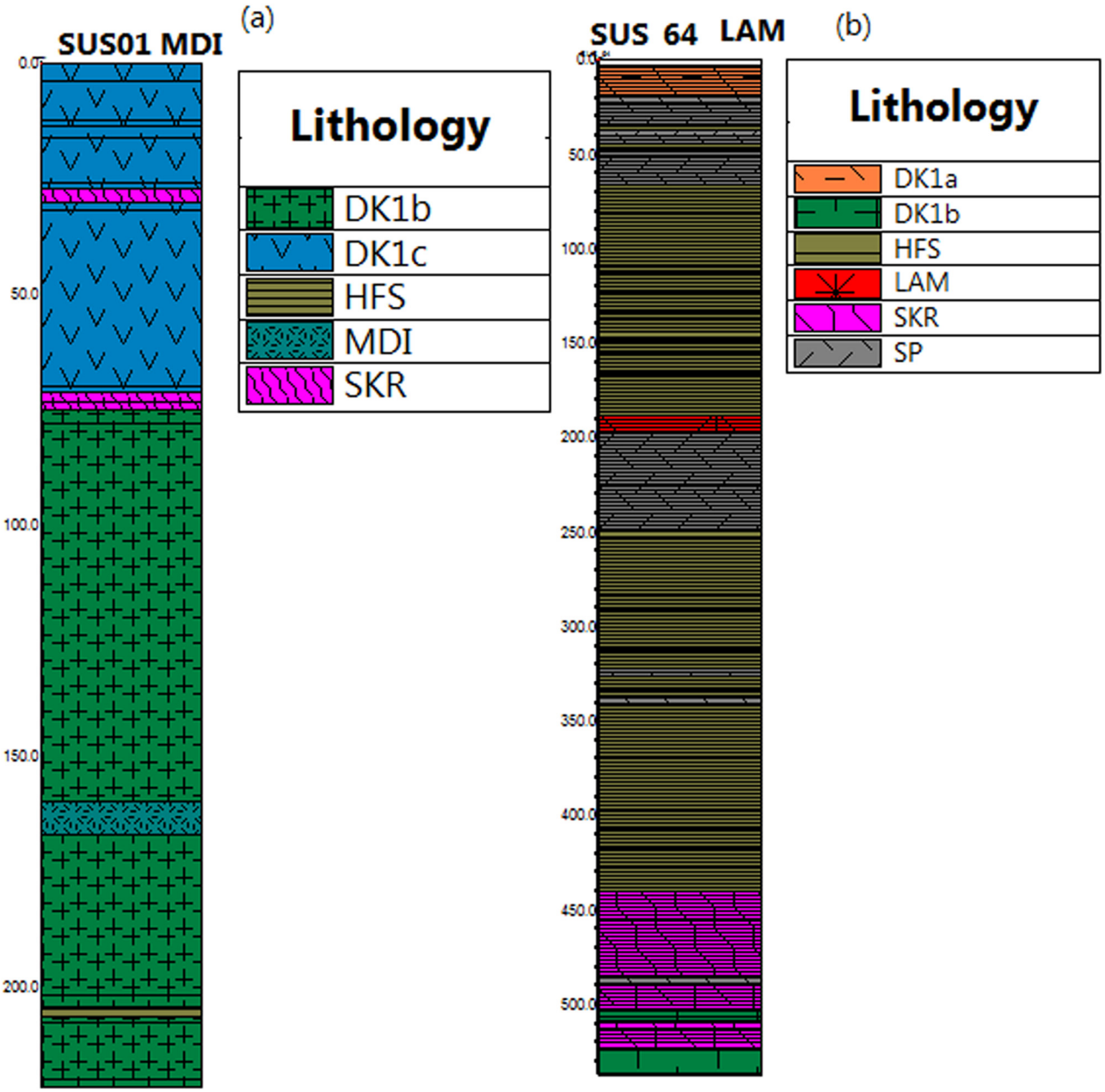

Figure 4: Borehole logging showing variety of rocks, including some not exposed within the Sungun mine. (a) MDI dyke. (b) LAM dyke. DK1a, DK1c and DK1b, quartz dioritic dykes separated in terms of alteration and relative time of emplacement; HFS, Hornfels; LAM, lamprophyric dykes; MDI, microdioritic dykes; SKR, skarn; SP, Sungun porphyritic body.

3.1.6 Gabbrodiorite dyke (DK2)

These dykes have not been observed inside the Sungun mine but are exposed outside the northeastern part of the pit. In these dykes, dark and shiny phenocrysts (1–1.5 mm) of clinopyroxene occur, which are not seen in the dykes exposed within the mine pit. The main minerals of this rock group are plagioclase (50–55%), clinopyroxene (25–30%) and amphibole (15–20%). Plagioclase forms subhedral oikocrysts (0.3–0.7 mm) containing inclusions of clinopyroxene, which have partly been altered and substituted by chlorite. Amphibole is subhedral with chlorite alteration and pseudomorphic calcite.

3.1.7 Diorite dyke (DK3)

These dykes are greenish in colour, with fresh and white plagioclase phenocrysts, which in some cases are converted to secondary epidote (Figure 5d). The main minerals of this

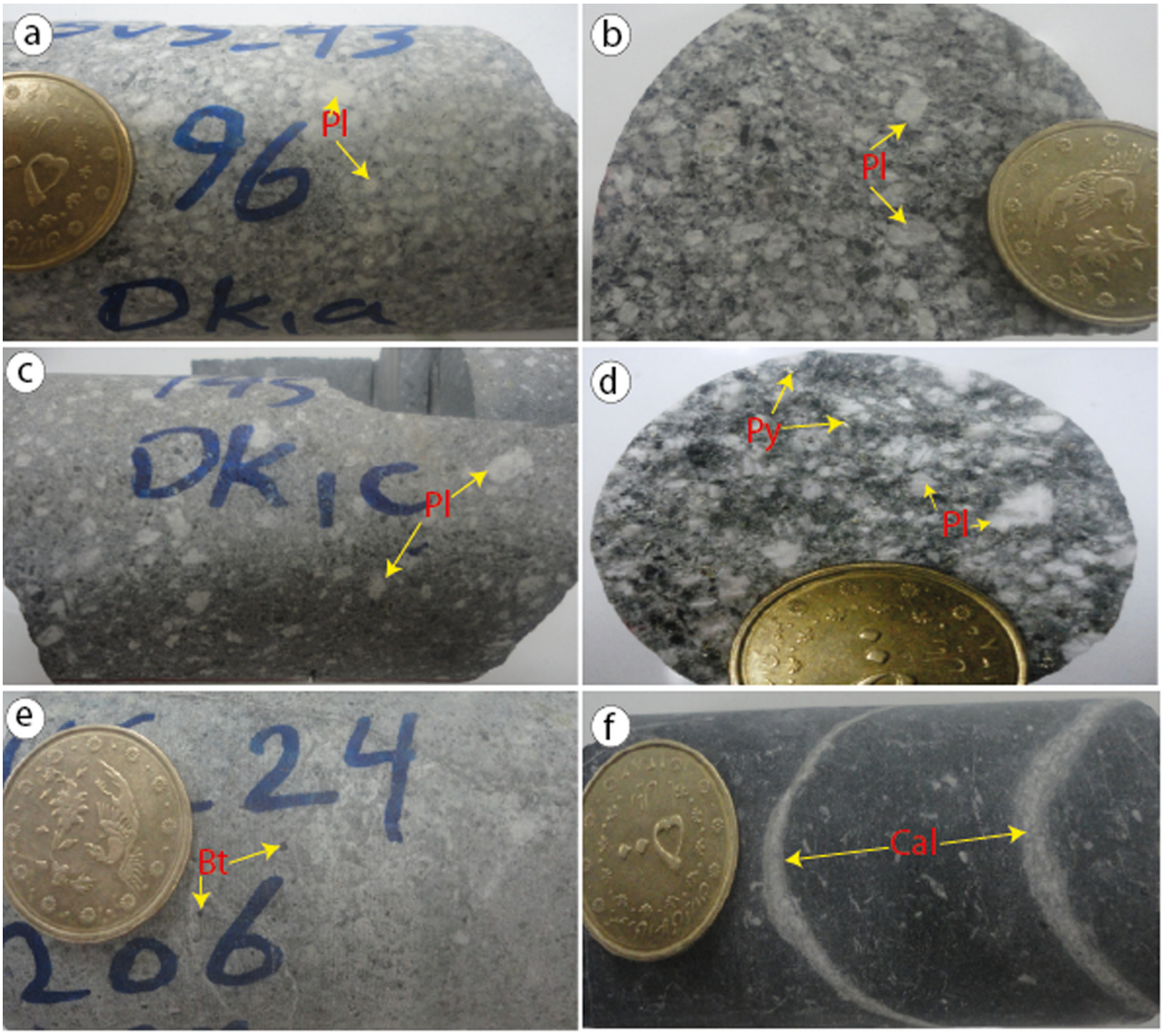

Figure 5: Hand examples of the post-mineralization dykes within the Sungun porphyry deposit: (a) quartz diorite dyke DK1a, (b) quartz diorite dyke DK1b, (c) quartz diorite dyke DK1c, (d) diorite dyke (DK3) with specific plagioclase and pyrite, (e) LAM dyke with biotite minerals and (f) MDI dyke with calcite veins.

rock group are plagioclase (50–55%) and amphibole (35–40%). Plagioclase generally occurs as subhedral to euhedral, fine-to-coarse-grained crystals, most of which have albite and Carlsbad twins (Figure 6d). Most amphibole phenocrysts are subhedral and show twinning (Figure 6d). The minor minerals in these dykes include orthoclase, quartz, sphene and apatite.

3.1.8 Trachytic to dacitic dykes (DK4)

In hand sample, these dykes are light grey to pink and leucocratic. The main minerals of this rock group include plagioclase (10–15%) and sanidine (10%). Plagioclase (1.5 mm) phenocrysts are euhedral to subhedral. Sanidine crystals form euhedral to subhedral microphenocrysts (0.7 mm) with the Carlsbad twins. Amphibole (5%) occurs as a minor mineral.

3.1.9 LAM dykes

The colour of this rock type is bright grey to green in hand samples. The rock is overall porphyritic with a microlytic groundmass (Figure 5e). The main minerals of this rock group are biotite (40–50%), plagioclase (20–30%) and

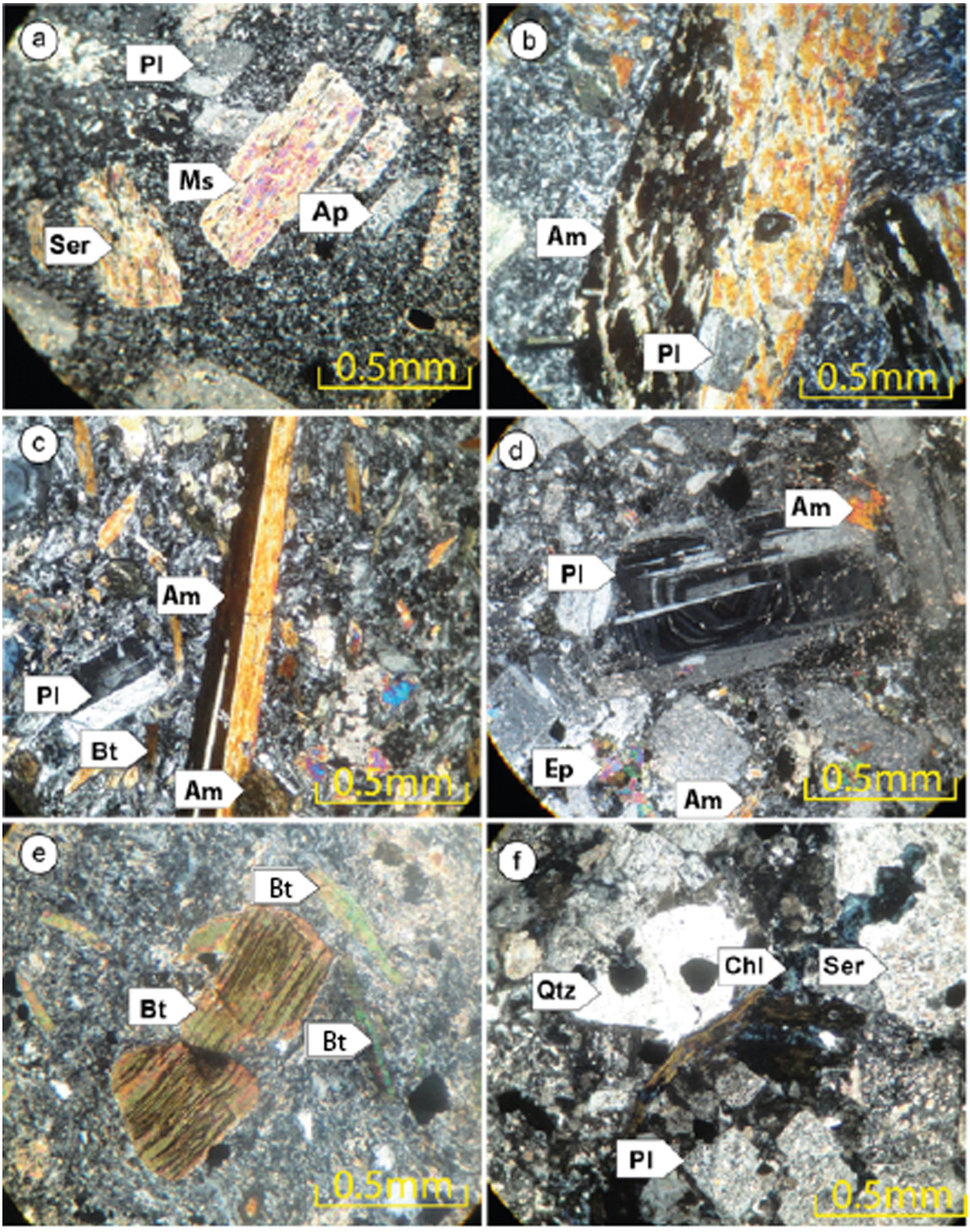

Figure 6: Microscopic sections of the post-mineralization Sungun dykes. (a) Biotite crystals have been altered to muscovite, along with plagioclase altered to sericite in quartz diorite dyke (DK1a); (b) amphibole phenocrysts with the Carlsbad twin in quartz diorite dyke (DK1b); (c) amphibole phenocrysts, plagioclase and biotite in DK1c; (d) Zoning plagioclase phenocrysts with amphibole in diorite dyke (DK3); (e) biotite phenocrysts in LAM dyke and (f) sericitized plagioclase with minerals of ferromagnesian chloride and quartz in dictation of MDI. All images are in XPL mode.

Table 2: Representative plagioclase analyses of the post-mineralization Sungun dykes

	DK1a			DK1b			DK1c			DK3			LAM		LAM			MDI		
Sample	**1***	**2***	**3***	**1***	**2***	**3***	**1***	**2***	**3***	**1***	**2***	**3***	**1**	**2**	**1***	**2***	**3***	**1***	**2***	**3***
SiO_2	68.71	68.56	69.63	62.75	61.94	61.55	58.93	57.42	57.69	55.47	56.41	56.56	66.13	61.97	68.92	68.77	68.2	67.01	67.7	66.77
TiO_2	0	0	0	0	0	0.01	0	0	0	0.05	0	0	0	0	0	0	0	0	0	0
Al_2O_3	20.43	20.19	20.52	21.71	20.73	22.49	25.1	26.95	26.45	27.44	26.83	26.36	18.04	18.67	20.46	20.51	20.59	19.72	20.05	20.41
Cr_2O_3	0	0	0	0	0	0	0	0	0	0	0	0	0	0	0	0	0	0	0	0
FeO	0.03	0.03	0.02	0.59	0.56	0.19	0.25	0.24	0.25	0.44	0.41	0.42	0.05	0.08	0.01	0.01	0.01	0.03	0.2	0.07
MnO	0	0	0	0	0.01	0	0	0	0	0	0.01	0	0	0	0	0	0	0.01	0	0.03
MgO	0	0	0	0.44	0.44	0.05	0	0	0	0.04	0.02	0.03	0.01	0.11	0	0	0	0.01	0.05	0.02
CaO	0.11	0.09	0.13	2.7	4.13	4.7	7.02	8.3	7.74	10.37	9.65	9.25	0	0.09	0.57	0.57	0.48	0.6	0.45	0.23
Na_2O	11.2	11.64	11.57	10.51	10.77	9.53	6.99	6.49	6.77	5.69	6.01	6.36	0.75	1.32	10.94	11.31	11.24	10.37	11.01	10.99
K_2O	0.07	0.1	0.08	0.39	0.33	1.02	0.52	0.39	0.44	0.48	0.62	0.6	16.09	15.78	0.11	0.11	0.17	0.23	0.33	0.56
Total	100.55	100.6	101.94	99.09	98.91	99.54	98.81	99.79	99.34	99.98	99.96	99.58	101.07	98.02	101.01	101.28	100.69	97.99	99.79	99.08
8(O)																				
Si	2.98	2.98	2.98	2.81	2.8	2.77	2.66	2.58	2.6	2.51	2.55	2.56	3.02	2.94	2.98	2.97	2.96	2.98	2.97	2.95
Ti	0	0	0	0	0	0	0	0	0	0	0	0	0	0	0	0	0	0	0	0
Al	1.04	1.03	1.03	1.15	1.11	1.19	1.34	1.43	1.41	1.46	1.43	1.41	0.97	1.04	1.04	1.04	1.05	1.03	1.04	1.06
Cr	0	0	0	0	0	0	0	0	0	0	0	0	0	0	0	0	0	0	0	0
Fe^{2+}	0	0	0	0.02	0.02	0.01	0.01	0.01	0.01	0.02	0.02	0.02	0	0	0	0	0	0	0.01	0
Mn	0	0	0	0	0	0	0	0	0	0	0	0	0	0	0	0	0	0	0	0
Mg	0	0	0	0.03	0.03	0	0	0	0	0	0	0	0	0.01	0	0	0	0	0	0
Ca	0	0	0.01	0.13	0.2	0.23	0.34	0.4	0.37	0.5	0.47	0.45	0	0	0.03	0.03	0.02	0.03	0.02	0.01
Na	0.94	0.98	0.96	0.91	0.95	0.83	0.61	0.57	0.59	0.5	0.53	0.56	0.07	0.12	0.92	0.95	0.95	0.89	0.94	0.94
K	0	0.01	0	0.02	0.02	0.06	0.03	0.02	0.03	0.03	0.04	0.03	0.94	0.96	0.01	0.01	0.01	0.01	0.02	0.03
Total	4.97	5	4.99	5.08	5.13	5.08	4.99	5	5.01	5.02	5.02	5.03	5	5.08	4.97	4.99	4.99	4.96	4.99	5
Or	0.43	0.55	0.43	2.09	1.64	5.24	3.02	2.28	2.56	2.69	3.47	3.33	93.38	88.35	0.65	0.64	0.98	1.4	1.87	3.22
Ab	99.05	99.03	98.97	85.74	81.16	74.46	62.37	57.26	59.73	48.48	51.15	53.6	6.62	11.23	96.55	96.68	96.74	95.53	95.97	95.66
An	0.51	0.41	0.6	12.17	17.2	20.29	34.61	40.46	37.72	48.83	45.38	43.08	0	0.42	2.8	2.68	2.28	3.07	2.15	1.12

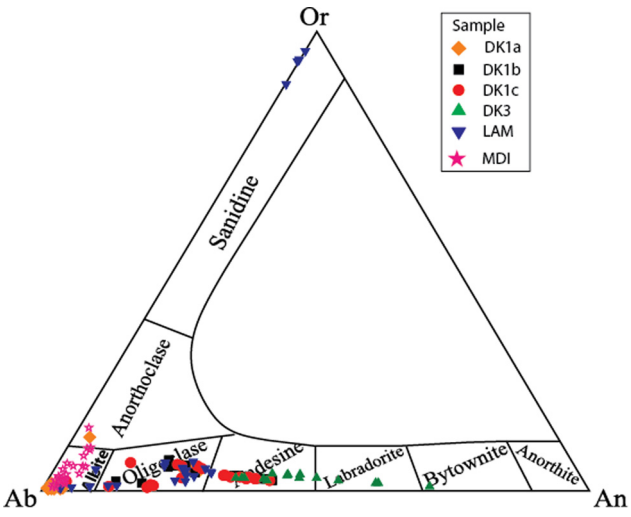

Figure 7: Classification of plagioclase minerals in the quartz diorite (DK1a, DK1b and DK1c), diorite (DK3), LAM and MDI dykes based on chemical composition [19].

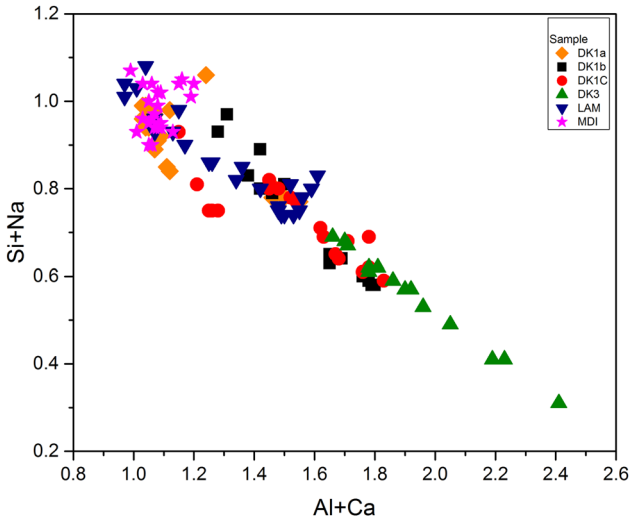

Figure 9: Al + Ca diagram against Si + Na, substitution mechanism in plagioclase in the quartz diorite (DK1a, DK1b and DK1c), diorite (DK3), LAM and MDI dykes.

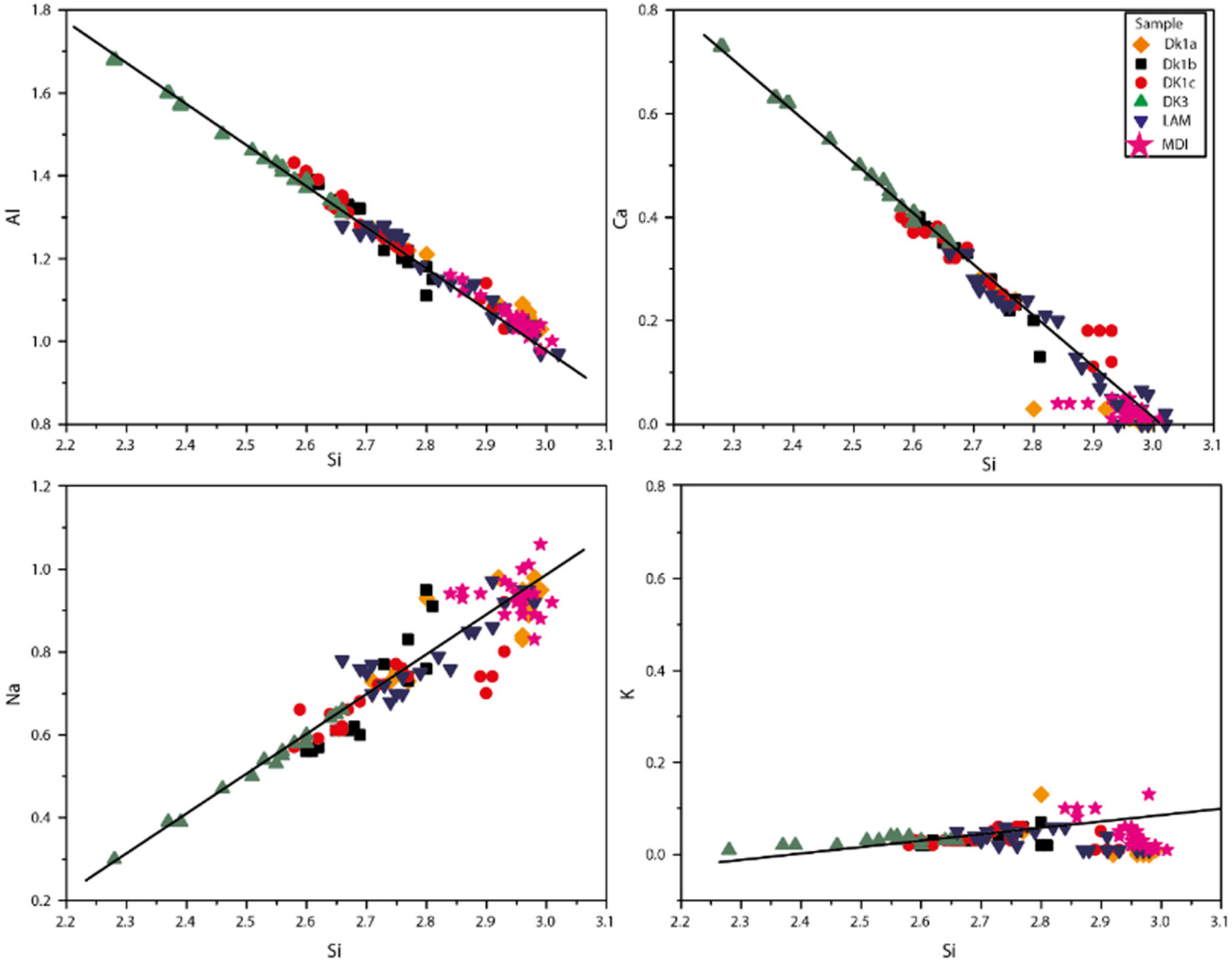

Figure 8: Variation of Na, Ca, Al and K with respect to Si (apfu) and changes in chemical composition of plagioclase in the quartz diorite (DK1a, DK1b and DK1c), diorite (DK3), LAM and MDI dykes.

Table 3: Results of the microprobe analyses of amphiboles within the Sungun dykes

	Dk1b				DK1c				DK3				LAM			
Sample	**b1**	**b2**	**b3**	**b4**	**c1**	**c2**	**c3**	**c4**	**3.10**	**3.20**	**3.30**	**3.40**	**L1**	**L2**	**L3**	**L4**
SiO_2	46.81	46.67	46.66	45.63	45.76	46.04	46.72	46.59	45.01	43.26	47.85	47.36	46.28	45.68	44.64	45.55
TiO_2	1.13	1.24	0.93	1.29	1.60	1.65	1.59	1.70	2.15	2.99	1.31	1.29	1.10	1.20	1.29	1.22
Al_2O_3	7.96	8.53	8.67	8.58	8.63	8.77	8.35	8.53	9.79	10.56	7.02	7.29	7.90	8.13	8.79	8.30
FeO	14.70	15.39	15.39	14.29	13.78	13.97	12.62	12.68	11.55	12.02	11.50	11.57	14.13	14.65	15.23	14.57
MnO	0.32	0.38	0.37	0.34	0.12	0.13	0.10	0.08	0.32	0.24	0.33	0.34	0.33	0.34	0.30	0.32
MgO	13.36	13.59	13.61	13.15	13.75	13.41	14.11	13.96	15.52	14.52	16.45	16.18	13.86	13.37	13.06	13.57
CaO	11.43	11.44	11.27	11.64	12.70	12.62	12.94	12.65	11.08	11.25	10.51	10.59	11.24	11.14	11.27	11.15
Na_2O	1.72	1.44	1.43	1.69	1.71	1.76	1.81	1.91	2.52	2.52	1.34	1.43	1.41	1.57	1.68	1.59
K_2O	1.02	1.06	1.02	0.98	0.09	0.07	0.06	0.04	0.78	1.02	0.40	0.41	0.87	0.96	0.98	0.93
Total	100.53	101.85	101.46	99.65	100.23	100.51	100.40	100.24	100.85	100.48	98.82	98.56	99.19	99.10	99.30	99.27
T																
Si	6.74	6.63	6.64	6.63	6.57	6.60	6.68	6.66	6.33	6.17	6.81	6.76	6.71	6.66	6.51	6.62
Al	1.26	1.37	1.36	1.37	1.44	1.41	1.32	1.34	1.62	1.77	1.18	1.23	1.29	1.34	1.49	1.39
Ti	0.00	0.00	0.00	0.00	0.00	0.00	0.00	0.00	0.04	0.06	0.02	0.01	0.00	0.00	0.00	0.00
Total	8.00	8.00	8.00	8.00	8.00	8.00	8.00	8.00	8.00	8.00	8.00	8.00	8.00	8.00	8.00	8.00
C																
Al	0.09	0.05	0.09	0.10	0.02	0.08	0.08	0.10	0.00	0.00	0.00	0.00	0.06	0.05	0.02	0.04
Ti	0.12	0.13	0.10	0.14	0.17	0.18	0.17	0.18	0.18	0.26	0.12	0.13	0.12	0.13	0.14	0.13
Fe^{3+}	0.96	1.11	1.17	0.97	1.06	0.99	0.86	0.88	1.42	1.31	1.25	1.26	1.07	1.10	1.23	1.16
Mg	2.87	2.88	2.89	2.85	2.94	2.86	3.01	2.98	3.26	3.09	3.49	3.45	3.00	2.90	2.84	2.94
Fe^{2+}	0.81	0.72	0.66	0.77	0.59	0.69	0.64	0.63	−0.06	0.12	0.12	0.12	0.65	0.69	0.63	0.61
Mn^{2+}	0.04	0.05	0.05	0.04	0.02	0.02	0.01	0.01	0.04	0.03	0.02	0.04	0.04	0.04	0.04	0.04
Total	4.89	4.94	4.95	4.87	4.81	4.81	4.78	4.79	4.84	4.81	5.00	5.00	4.93	4.92	4.89	4.92
B																
Ca	1.76	1.74	1.72	1.81	1.95	1.94	1.98	1.94	1.67	1.72	1.60	1.62	1.75	1.74	1.76	1.74
Na	0.24	0.26	0.28	0.19	0.05	0.06	0.02	0.06	0.33	0.28	0.37	0.38	0.25	0.26	0.24	0.27
Total	2.00	2.00	2.00	2.00	2.00	2.00	2.00	2.00	2.00	2.00	1.99	2.00	2.00	2.00	2.00	2.00
A																
Na	0.24	0.14	0.11	0.29	0.43	0.43	0.48	0.47	0.36	0.42	0.00	0.02	0.14	0.18	0.24	0.18
Ca	0.00	0.00	0.00	0.00	0.00	0.00	0.00	0.00	0.00	0.00	0.00	0.00	0.00	0.00	0.00	0.00
K	0.19	0.19	0.19	0.18	0.02	0.01	0.01	0.01	0.14	0.19	0.07	0.08	0.16	0.18	0.18	0.17
Total	0.43	0.33	0.30	0.47	0.44	0.44	0.49	0.48	0.50	0.60	0.07	0.09	0.30	0.36	0.42	0.36

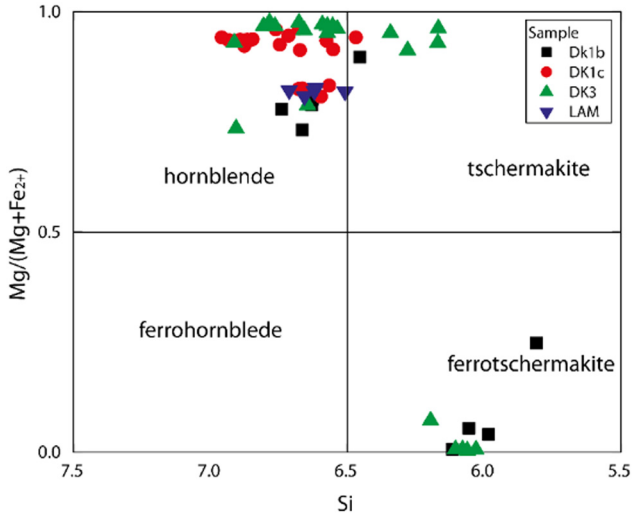

Figure 10: Amphibole composition in the Si vs the cationic ratio of $Mg/(Mg + Fe^{2+})$ diagram [20] in the quartz diorite (DK1b and DK1c), diorite (DK3) and LAM dykes.

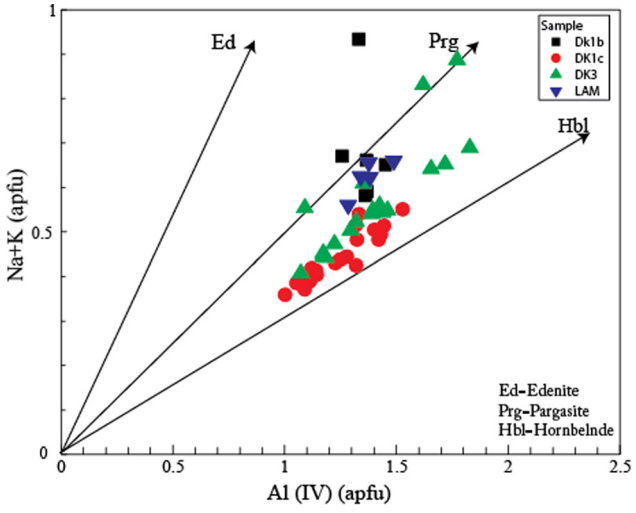

Figure 11: Edenite–pargasite and hornblende substitutions based on Al^{IV} values relative to (Na + K) for the quartz diorite (DK1b and DK1c), diorite (DK3) and LAM dykes [20].

amphibole (5–10%). Biotite phenocrysts (1.3 mm) are euhedral to subhedral (Figure 6e). Plagioclase forms microlites within the groundmass with only rare phenocrysts (0.3–1 mm). Amphibole forms euhedral to subhedral phenocrysts to microphenocrysts (1.1 mm) with simple twins (Figure 6e). Orthoclase is rare and occurs mostly as subhedral microphenocrysts with perthitic exsolution in the groundmass. The minor mineral phases in these dykes include apatite, zircon and quartz. Rare clinopyroxene microlites form in the groundmass and some secondary pyrite may be present. According to the mineralogical and geochemical evidence, the studied LAM samples are of kersantite type and are calc-alkaline [18].

3.1.10 MDI dykes

These dykes are porphyritic with a microlytic groundmass, light grey to yellowish cream in colour and strongly altered (Figure 5f). The main minerals include phenocrysts of plagioclase (25–30%) and ferromagnesian minerals (10–15%). Plagioclase is altered to sericite, epidote and calcite (Figure 6f). Ferromagnesian minerals are subhedral and are highly altered to chlorite, epidote and muscovite (Figure 6f). Amorphous quartz occurs interstitially to other phases (Figure 6f).

3.2 Plagioclase chemistry

The results of the microprobe analysis and the structural composition of plagioclase are presented in Table 2. The composition of plagioclase varies from relatively calcic labradorite to andesine in the diorite (DK3) to more sodic andesine to oligoclase in the quartz diorite dykes (DK1a, DK1b and DK1c). LAM contains both plagioclase and alkali feldspar as oligoclase and orthoclase. Feldspars in the MDI and some in the LAM and quartz diorite dykes DK1a are almost pure albite (Figure 7).

The use of Si against elements such as Al, Ca, Na and K can give information on the changes in the chemical composition of the plagioclase. The amount of Al increases with increasing Ca, and a positive correlation is found between Si and K and Na. On the other hand, with increasing Si, the amount of Ca and Al decreases (Figure 8). In plagioclase, the tetrahedral site is filled by Si and Al and a large cationic site is filled by Na, Ca and K and sometimes by Ba. The changes in the chemical composition of the plagioclase are influenced not only by the substitution of Na and Ca but also by the substitution of Al instead of Si in the four-strand network. Thus, the substitution in the plagioclase is controlled by the Na + Si ⇔ Ca + Al relationship shown in Figure 9.

3.3 Amphibole chemistry

The representative amphibole compositions are presented in Table 3 with cations calculated on the basis of 23 oxygen atoms. Based on the classification of [20], the amphibole in the Sungun dykes are a combination of hornblende-tschermakite and ferrotschermakite (Figure 10). These can be further characterized based

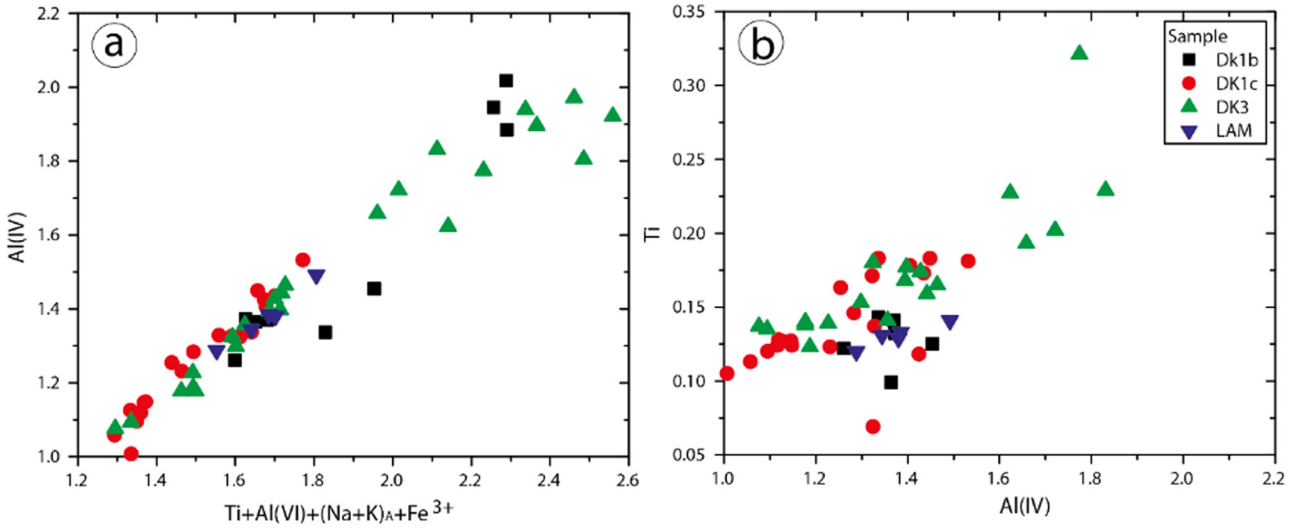

Figure 12: (a) Almost perfect linear variation of Al^{IV} with $Al^{VI} + Fe^{3+} + Ti + (Na + K)$ [21]. (b) Ti diagrams relative to Al^{IV} in amphiboles. All amphiboles have less than 0.5 Ti atom in the structural formula.

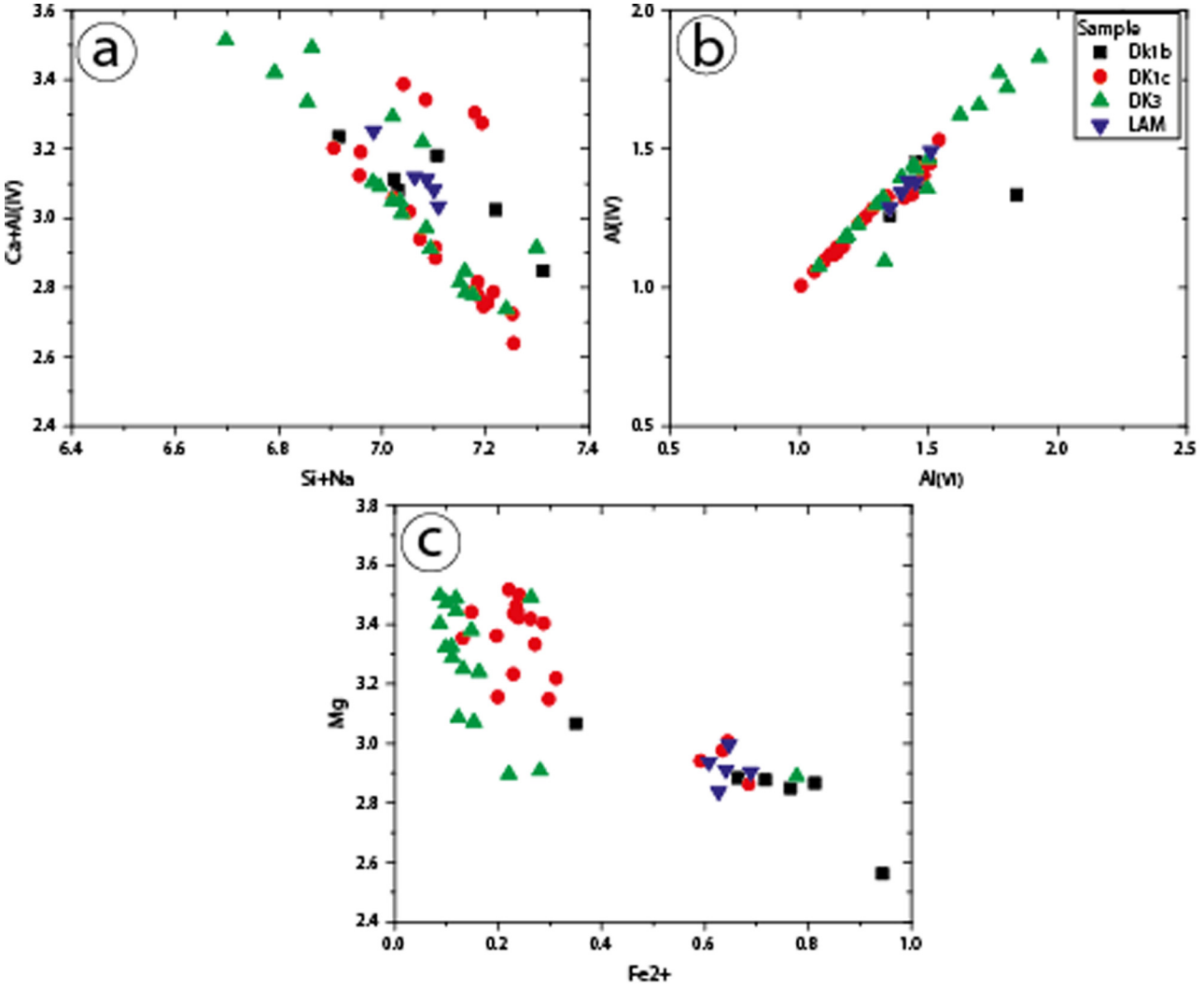

Figure 13: (a) Si + Na diagram vs Ca + ^{IV}Al [23]. (b) Al (total) variation have linear correlation with Al^{IV} in the analysed amphiboles [22]. (c) Mg vs Fe^{2+}.

Table 4: Results of the microprobe analysis of biotite in the quartz diorite (DK1c) and LAM dykes

	DK1c							LAM						
Sample	**AB1***	**AB2***	**AB3***	**AB4***	**AB5***	**AB6**	**AB7**	**a1**	**a2**	**a3**	**a4**	**a5**	**a6**	**a7**
SiO_2	37.63	37.78	37.96	37.56	37.37	36.88	36.49	38.14	38.06	37.95	37.98	38.27	37.67	37.37
TiO_2	4.02	4.35	4.34	4.37	4.26	4.32	4.22	3.68	3.52	3.73	3.53	3.84	3.91	3.89
Al_2O_3	14.28	14.17	14.31	14.2	14.3	14.13	14.12	14.86	14.4	14.41	14.52	14.59	13.93	14
Cr_2O_3	0	0	0	0	0	0	0	0	0	0	0	0	0	0
FeO	13.74	13.74	13.52	13.66	13.85	13.48	13.5	16.13	16.16	16.21	15.19	14.49	15.72	15.63
MnO	0.11	0.16	0.13	0.14	0.15	0.13	0.15	0.08	0.08	0.07	0.06	0.06	0.06	0.1
MgO	16.94	16.24	16.61	16.56	16.4	15.51	15.6	14.94	14.6	14.55	15.2	15.43	14.87	14.7
CaO	0.07	0.09	0.11	0.03	0.04	0.01	0.02	0	0.01	0.02	0.01	0	0.01	0.01
Na_2O	0.38	0.45	0.48	0.42	0.4	0.56	0.58	0.01	0.02	0.04	0.03	0.02	0.02	0.01
K_2O	7.77	8.22	8.36	8.16	7.83	8.3	8.14	9.38	9.3	9.29	9.52	9.4	9.33	9.42
BaO	0	0	0	0	0	0	0	0	0	0	0	0	0	0
F	0.22	0.61	0.43	0.38	0.31	0.37	0.36	0.53	0.35	0.44	0.91	0.81	0.47	0.64
Cl	0.12	0.13	0.13	0.13	0.13	0.12	0.12	0.18	0.18	0.19	0.19	0.18	0.18	0.19
O = F, Cl	0.12	0.29	0.21	0.19	0.16	0.18	0.18	0.26	0.19	0.23	0.43	0.38	0.24	0.31
Total	95.4	96.23	96.59	95.8	95.2	93.99	93.48	98.19	96.87	97.13	97.53	97.47	96.41	96.27
Formula 11(O)														
Si	2.77	2.78	2.78	2.77	2.77	2.78	2.76	2.79	2.81	2.8	2.8	2.81	2.8	2.79
Ti	0.22	0.24	0.24	0.24	0.24	0.24	0.24	0.2	0.2	0.21	0.2	0.21	0.22	0.22
Al	1.24	1.23	1.23	1.23	1.25	1.25	1.26	1.28	1.25	1.25	1.26	1.26	1.22	1.23
Cr	0	0	0	0	0	0	0	0	0	0	0	0	0	0
Fe^{3+}	0.08	0.08	0.08	0.08	0.09	0.08	0.09	0.1	0.1	0.1	0.09	0.09	0.1	0.1
Fe^{2+}	0.76	0.76	0.74	0.76	0.77	0.76	0.77	0.89	0.9	0.9	0.84	0.8	0.88	0.88
Mn	0.01	0.01	0.01	0.01	0.01	0.01	0.01	0	0.01	0	0	0	0	0.01
Mg	1.86	1.78	1.81	1.82	1.81	1.74	1.76	1.63	1.61	1.6	1.67	1.69	1.65	1.64
Ca	0.01	0.01	0.01	0	0	0	0	0	0	0	0	0	0	0
Na	0.05	0.06	0.07	0.06	0.06	0.08	0.08	0	0	0.01	0	0	0	0
K	0.73	0.77	0.78	0.77	0.74	0.8	0.79	0.87	0.88	0.88	0.9	0.88	0.89	0.9
Ba	0	0	0	0	0	0	0	0	0	0	0	0	0	0
Total	7.74	7.74	7.75	7.74	7.73	7.75	7.76	7.76	7.75	7.75	7.77	7.75	7.76	7.77
$Mg/Fe^{+}Mg$	0.69	0.68	0.69	0.68	0.68	0.67	0.67	0.62	0.62	0.62	0.64	0.65	0.63	0.63

on their sodium and potassium content. The amphibole samples of the quartz diorite dykes (DK1b and DK1c), diorite (DK3) and LAM show cationic replacement from hornblende to pargasite (Figure 11). The linear arrays in Figure 12 indicate that the chemical variation in the amphiboles in these rocks depends on the amount of Al^{IV} and the substitution of (Na + K), Ti, Al^{VI} and Fe^{3+} cations in the octahedral sites [21]. In the Ti vs Al^{IV} diagram, all amphiboles have less than 0.5 Ti atoms in the structural formula (Figure 12b). The Al decrease correlated with a decrease in Ti is due to the increase of Si in the crystalline structure and likely represents the enrichment of Si as magmatic evolution progresses. Figure 13a shows that the studied amphiboles were rich in Ca + Al^{IV} and that the Ca + Al^{IV} = Si + Na substitution was an important factor controlling their composition. The linear relationship between Al^{IV} and Al^{VI} is indicative of the systematic difference in the amount of aluminium in the amphiboles (Figure 13b) [22]. The substitution Mg = Fe^{2+} is also important for the amphiboles examined (Figure 13c).

3.4 Biotite chemistry

The results of the analysis of biotite minerals found in the quartz diorite dykes (DK1c) and LAM are presented in Table 4. Cationic values were calculated based on 11 oxygen atoms and their structural formula was determined according to the general formula of the mica ($I\ M_{2-3}\ \square_{1-0}\ T_4\ O_{10}\ A_2$). Based on the Fe/(Fe + Mg) vs Si diagram [24], the biotite in DK1c and LAM dykes is magnesium biotite and magnesium–phlogopite, respectively (Figure 14a). According to the classification of [25] (Figure 14b), the studied biotite spans the boundary between the primary and the re-equilibrated primary

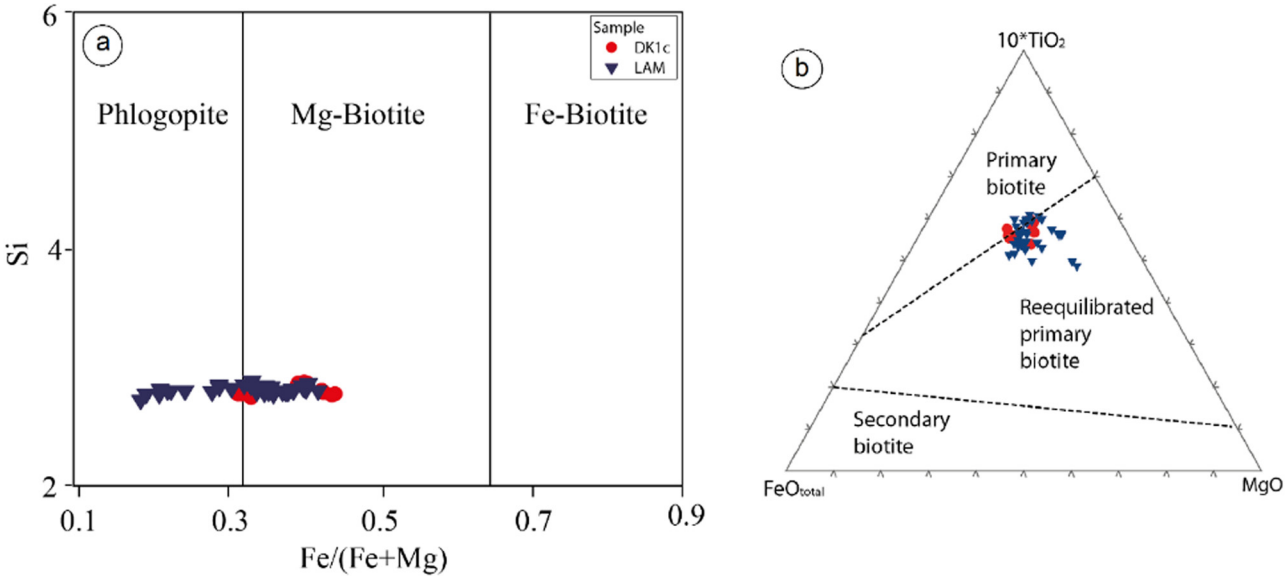

Figure 14: Composition of biotite in the quartz diorite and LAM dykes. (a) Fe/(Fe + Mg) vs Si [24]. (b) FeO–10*TiO_2–MgO ternary diagram [25,26].

biotite. The amount of Al^{VI} in biotite is one of the important criteria for the study of their properties, with values of Al^{VI} < 1 being characteristic of magmatic biotite [26], which is applicable to the biotite studied here (0.013).

3.5 White mica chemistry

The results of the microprobe analyses of white mica in DK1a are presented in Table 5. In this table, the formula for white

Table 5: Results of the microprobe analysis of white mica mineral in the quartz diorite dyke (DK1a)

Sample	Mst1	Mst2	Mst3	Mst4	Mst5	Msa1	Msa2	Msa3	Msa4	Msa5	Msa6	Msa7	Msa8	Msa9	Msa10
SiO_2	48.87	49.44	49.42	49.10	51.04	50.87	48.92	50.31	50.41	46.56	50.23	50.07	50.62	46.65	52.22
TiO_2	0.06	0.09	0.09	0.10	0.10	0.28	0.11	0.22	0.16	0.17	0.41	0.22	0.33	0.18	0.30
Al_2O_3	30.78	32.37	30.82	30.60	31.27	30.01	32.57	30.91	30.70	31.18	28.31	31.02	30.65	27.65	31.15
Cr_2O_3	0.00	0.00	0.00	0.00	0.00	0.00	0.00	0.00	0.00	0.00	0.00	0.00	0.00	0.00	0.00
FeO	1.91	1.98	2.72	1.87	1.96	3.33	2.69	2.23	2.26	4.77	4.24	2.41	2.65	5.53	1.95
MnO	0.01	0.01	0.01	0.00	0.01	0.01	0.03	0.00	0.01	0.03	0.06	0.00	0.00	0.06	0.00
MgO	1.17	1.30	1.71	1.96	1.38	1.82	1.26	1.79	1.85	3.49	2.68	1.72	1.86	4.54	2.08
CaO	0.02	0.03	0.02	0.01	0.03	0.07	0.09	0.07	0.03	0.07	0.03	0.07	0.04	0.08	0.06
Na_2O	0.00	0.00	0.00	0.00	0.00	0.00	0.05	0.04	0.03	0.00	0.02	0.03	0.02	0.01	0.05
K_2O	10.21	8.88	8.39	9.44	9.39	10.10	9.97	9.67	9.83	8.77	10.09	9.74	9.93	7.57	9.53
Total	93.03	94.10	93.18	93.08	95.18	96.49	95.69	95.24	95.28	95.04	96.07	95.28	96.10	92.27	97.34
Si	3.32	3.29	3.32	3.31	3.36	3.35	3.24	3.33	3.33	3.13	3.34	3.31	3.33	3.23	3.36
Ti	0.00	0.00	0.00	0.01	0.00	0.01	0.01	0.01	0.01	0.01	0.02	0.01	0.02	0.01	0.01
Al	2.46	2.54	2.44	2.43	2.42	2.33	2.54	2.41	2.39	2.47	2.22	2.42	2.38	2.26	2.36
Cr	0.00	0.00	0.00	0.00	0.00	0.00	0.00	0.00	0.00	0.00	0.00	0.00	0.00	0.00	0.00
Fe^{3+}	0.00	0.00	0.00	0.00	0.00	0.00	0.00	0.00	0.00	0.00	0.00	0.00	0.00	0.00	0.00
Fe^{2+}	0.11	0.11	0.15	0.11	0.11	0.18	0.15	0.12	0.12	0.27	0.24	0.13	0.15	0.32	0.10
Mn	0.00	0.00	0.00	0.00	0.00	0.00	0.00	0.00	0.00	0.00	0.00	0.00	0.00	0.00	0.00
Mg	0.12	0.13	0.17	0.20	0.14	0.18	0.12	0.18	0.18	0.35	0.27	0.17	0.18	0.47	0.20
Ca	0.00	0.00	0.00	0.00	0.00	0.00	0.01	0.00	0.00	0.01	0.00	0.00	0.00	0.01	0.00
Na	0.00	0.00	0.00	0.00	0.00	0.00	0.01	0.01	0.00	0.00	0.00	0.00	0.00	0.00	0.01
K	0.88	0.75	0.72	0.81	0.79	0.85	0.84	0.82	0.83	0.75	0.86	0.82	0.83	0.67	0.78
Total	6.89	6.82	6.81	6.87	6.82	6.90	6.91	6.87	6.88	7.00	6.95	6.88	6.89	6.97	6.84

Table 6: Results of the microprobe analysis of chlorite minerals in the quartz diorite (DK1a, DK1b and DK1c), diorite (DK3) and MDI dykes

Sample no	DK1a			DK1b		DK1c		DK3		MDI	
Point No	1	2	1	2	1	2	1	2	1	2	3
SiO_2	27.11	27.03	30.82	31.51	36.11	34.52	27.71	28.03	25.66	27.71	26.21
TiO_2	0.03	0.01	0	0.03	0.37	0.92	0.03	0.12	0.06	0.02	0.16
Al_2O_3	21.45	21.76	17.94	18.13	16.65	14.75	20.1	19.79	20.26	17.92	18.93
FeO	23.39	22.93	15.87	16.66	13.17	11.49	18.76	17.99	30.29	29.34	30.35
MnO	0.14	0.17	0.38	0.46	0.04	0.04	0.55	0.5	0.53	0.5	0.43
MgO	15.94	15.86	21.41	21.74	20.82	19.81	19.85	20.61	11.11	13.17	11.27
CaO	0.09	0.04	0.33	0.28	0.31	0.43	0.1	0.14	0.08	0.08	0.04
Na_2O	0	0	0	0	0.04	0.2	0	0	0	0	0
K_2O	0	0	0.02	0.03	1.7	6.08	0.01	0.03	0.08	0.02	0.16
F	0.25	0.14	0.21	0.31	0	0	0	0.05	0	0	0.14
Cl	0.01	0	0.02	0.02	0	0	0.01	0.01	0.02	0.01	0.01
O=F	0.1	0.06	0.09	0.13	0	0	0	0.02	0	0	0.06
O=Cl	0	0	0	0	0	0	0	0	0	0	0
Total	88.51	88	87.09	89.3	89.21	88.24	87.12	87.29	*88.08*	*88.76*	*87.76*
Si	2.8	2.79	3.1	3.1	3.47	3.45	2.83	2.85	2.77	2.94	2.85
Ti	0	0	0	0	0.03	0.07	0	0.01	0	0	0.01
Al	2.61	2.65	2.13	2.1	1.88	1.74	2.42	2.37	2.58	2.24	2.42
$Fe^{(2+)}$	2.02	1.98	1.33	1.37	1.06	0.96	1.61	1.53	2.73	2.61	2.76
Mn	0.01	0.02	0.03	0.04	0	0	0.05	0.04	0.05	0.05	0.04
Mg	2.45	2.44	3.21	3.19	2.98	2.95	3.03	3.13	1.79	2.09	1.83
Ca	0.01	0	0.04	0.03	0.03	0.05	0.01	0.01	0.01	0.01	0
Na	0	0	0	0	0.01	0.04	0	0	0	0	0
K	0	0	0	0	0.21	0.77	0	0	0.01	0	0.02
F	0.08	0.05	0.07	0.1	0	0	0	0.02	0	0	0.05
Cl	0	0	0	0	0	0	0	0	0	0	0
OH	7.92	7.95	7.93	7.9	8	8	8	7.98	8	8	7.95
Al(IV)	1.2	1.21	0.9	0.9	0.53	0.55	1.17	1.15	1.23	1.06	1.15
Al(VI)	1.4	1.44	1.22	1.21	1.35	1.18	1.26	1.23	1.35	1.19	1.27

mica is calculated based on 11 oxygen atoms. Generally, the oxide totals for this mineral is low (between 92.29 and 97.34), due to the presence of OH in the mineral network, which has the general formula $KAl_3Si_3O_{10}$ $(OH)_2$. According to the SiO_2-Al_2O_3-FeO+MgO diagram, white mica in DK1a shows a solid solution between muscovite and celadonite, with a greater proportion of the latter (Figure 15a). According to the classification of [27], mica in DK1a is secondary (Figure 15b). Zen [28] also expressed FeO and TiO_2 values for magmatic micas ranging from 4 to 6 wt% and more than 0.4 wt%, respectively. In most of our samples, the FeO and TiO_2 abundances for mica in DK1a dyke are 1.90–3.33 wt% and 0.06–0.33 wt%, respectively, consistent with a secondary origin.

3.6 Chemistry of chlorite

The oxide totals of chlorite are between 87 wt% and 89 wt %, due to the presence of OH in the mineral with the generalized structural formula (Mg, Fe^{2+}, Fe^{3+}, Mn, $Al)_6$ $((Si, Al)_4$ $O_{10})$ $(OH)_8$. The cation component calculations are based on 14 oxygen atoms, and the results are presented in Table 6. Based on the Si vs Mg/(Mg + Fe) discrimination diagram, the chemical composition of the chlorite in the quartz diorite (DK1a and DK1b), diorite (DK3) and MDI dykes falls in the range of pycnochlorite field, and in the dyke DK1c, it is within the pennine field (Figure 16).

3.7 Epidote chemistry

Epidote, which is one of the index minerals in propylitic alteration, has been identified in the studied area. The epidote formula is based on eight cations and 12.5 oxygen atom. All Fe atoms in the composition of the decomposed epidotes are considered as Fe^{3+}. In general, the structural formula of the epidote obtained from feldspar and ferromagnesian minerals are $Ca_{1.93}$ $(Al_{2.17}, Fe_{0.86})$ $3Si_3O_{13}H$ and Ca_2 $(A_{l2.22}, Fe_{0.89})$ $3Si_3O_{13}H$, respectively.

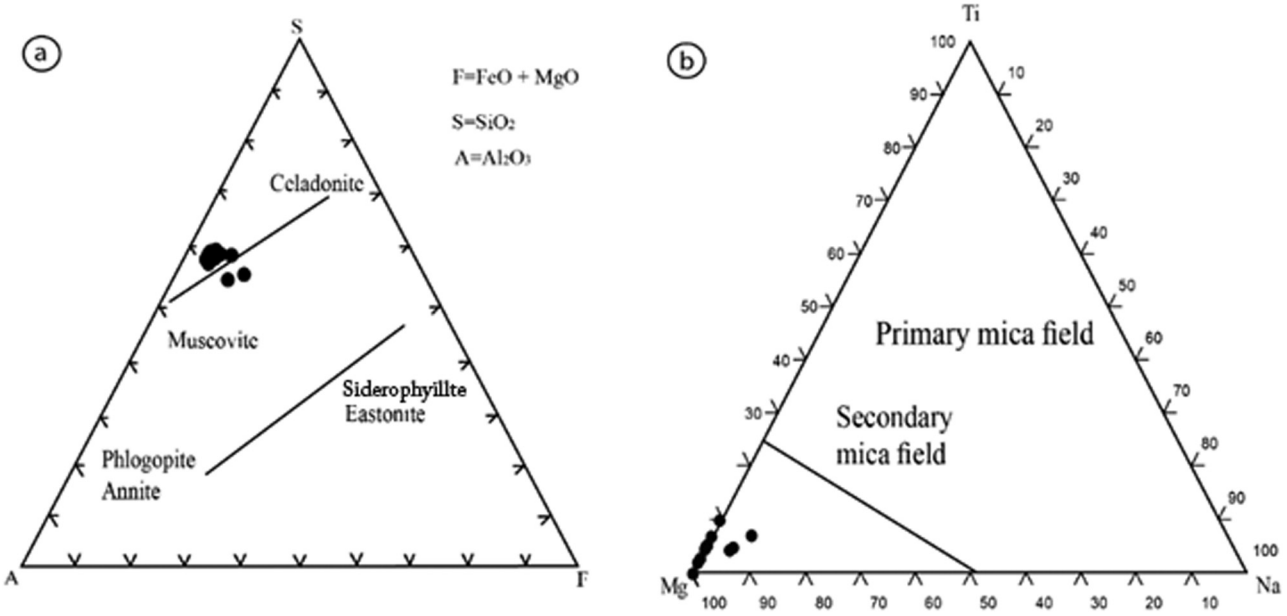

Figure 15: (a) Classification of the white mica of the quartz diorite dykes (DK1a) based on their chemical composition [19]. (b) Distinction of primary white mica (magmatic) from alteration types [27].

Magmatic epidote can be differentiated from secondary epidote by petrographic studies, textural relations and alteration effects, as well as chemical criteria. Optical detection of the series clinozoisite–epidote is difficult because of variable mineral colour. Therefore, to distinguish epidote, clinozoisite and zoisite, we used chemical analyses of the minerals. The epidote group minerals are divided into three groups based on the XFe^{3+} [$Fe^{3+}/(Fe^{3+} + Al^{3+} - 2 + Cr^{3+})$] ratio on the M3 site in the structural formula (Figure 17a) and the amount of XFe^{3+} in epidote ($XFe^{3+} > 0.5$), clinozoisite ($0.15 < XFe^{3+} < 0.5$) and zoisite ($XFe^{3+} < 0.15$) [31]. The amount of XFe^{3+} in the epidote of the LAM dykes in the region is greater than 0.5 (Tables 7 and 8). The Fe^{3+} vs Al^{3+} diagram shows that all the case study samples are located within the epidote range (Figure 17b).

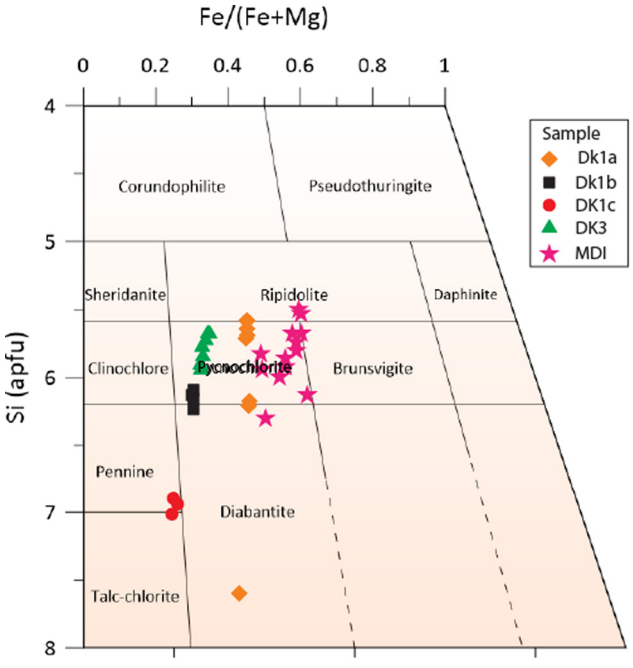

Figure 16: Variation of Si in relation to Fe/(Mg + Fe) in the chlorite composition of the quartz diorite (DK1a, DK1b and DK1c), diorite (DK3) and MDI dykes [29].

As mentioned, one of the most abundant secondary minerals in the region is epidote. Magmatic epidote can be differentiated from alteration epidote by the percentage of pistacite. Magmatic epidotes have a pistacite percentage of 23–27% [32]. High pistacite content expresses high oxygen fugacity [33]. This mineral is one of the most important minerals containing Fe^{3+}. Therefore, it provides valuable information on the oxygen extinction and the conditions for oxidation of a rock. Tables 7 and 8 present the results of the analysis of this mineral with the calculation of its structural formula. Where the composition is known, the percentage of pistacite [34] can be calculated to determine the epidote type more reliably than using textural criteria, based on the formula $P_s = 100*Fe^{3+}/(Fe^{3+} + Al)$. The average percentage of pistacite (P_s) in epidotes obtained from feldspar and ferromagnesian (mafic) minerals in

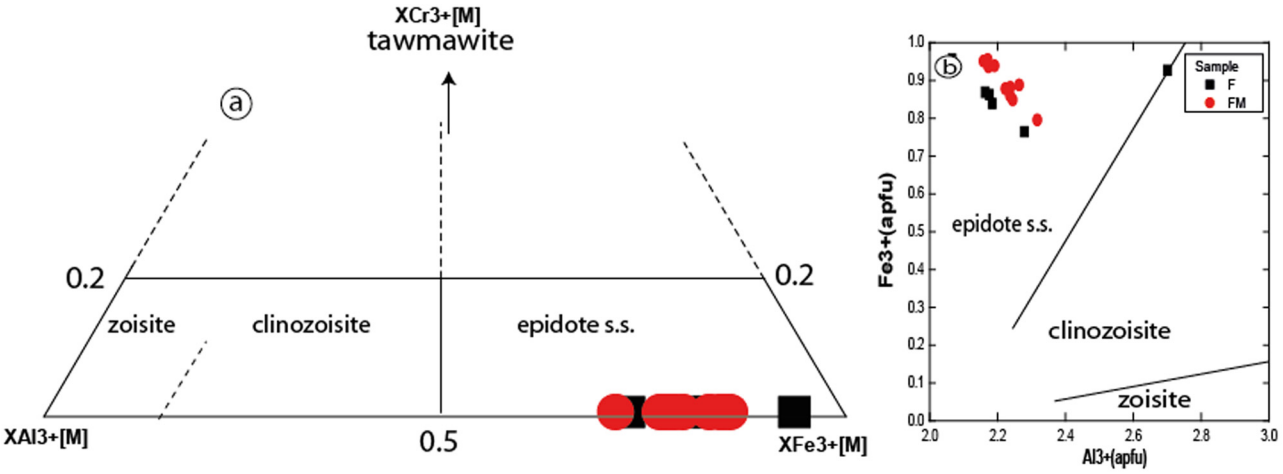

Figure 17: (a) Classification of minerals in the epidote group of the studied area on a triangular diagram based on [30]. ($XFe^{3+} = Fe^{3+}/(Fe^{3+} + Al^{3+} - 2 + Cr^{3+})$, $XCr^{3+} = Cr^{3+}/(Fe^{3+} + Al^{3+} - 2 + Cr^{3+})$, $XAl^{3+} = (Al^{3+} - 2)/(Fe^{3+} + Al^{3+} - 2 + Cr^{3+})$. (b) Fe^{3+} vs Al^{3+}.

the LAM dykes is 27–33% and 25–30%, respectively, whereas the P_s in the secondary epidotes resulting from saussuritization of plagioclase is between 24% and 50% (Figures 18 and 19). Also, the amount of TiO_2 in epidotes produced by ferromagnesian (mafic) minerals is between 0 and 0.05 based on the results in [35]. Therefore, the epidote of this area can be classified in the same category according to the petrographic studies and their composition.

Table 7: Results of the spot analysis of the epidote of plagioclase alteration with the calculation of its structural formula (LAM)

Sample	FD-Ep1-1	FD-Ep1-2	FD-Ep1-3	FD-Ep1-4	FD-Ep1-5
SiO_2	38.09	37.56	37.58	37.81	37.46
Al_2O_3	23.48	23.01	23.21	24.42	21.87
Fe_2O_3	14.13	14.47	14.41	12.84	15.86
CaO	22.78	22.49	22.52	22.69	22.73
SrO	0.46	0.49	0.51	0.36	0.20
BaO	0.00	0.00	0.00	0.00	0.00
Na_2O	0.00	0.00	0.00	0.00	0.00
K_2O	0.00	0.00	0.00	0.00	0.01
Rb_2O	0.02	0.00	0.02	0.04	0.01
P_2O_5	0.04	0.07	0.14	0.02	0.01
Total	99.00	98.08	98.39	98.18	98.15
Si	3.01	3.00	2.99	2.99	3.00
Al	2.18	2.16	2.18	2.28	2.07
Fe	0.84	0.87	0.86	0.76	0.96
Ca	1.93	1.92	1.92	1.93	1.95
Sr	0.02	0.02	0.02	0.02	0.01
Ba	0.00	0.00	0.00	0.00	0.00
Na	0.00	0.00	0.00	0.00	0.00
K	0.00	0.00	0.00	0.00	0.00
Rb	0.00	0.00	0.00	0.00	0.00
P	0.00	0.00	0.01	0.00	0.00
Sum	7.98	7.98	7.98	7.98	7.99
P_s	29.92	30.86	30.59	27.16	33.98
XFe^{3+}	0.82	0.84	0.83	0.73	0.94

3.8 Determination of tectonic environment using amphibole and biotite

3.8.1 Amphibole

To evaluate the character of the magma that formed the post-mineralization dykes in the Sungun area, we used the variation in the amphibole chemical composition and the Al_2O_3 and MgO vs TiO_2 variation diagrams [36]. Based on these discriminant graphs, the samples were found to be mostly subalkaline (Figure 20). Additionally, Al^{IV} can be employed as a discriminant for the tectonomagmatic environment of amphibole formation. The amphiboles having Al^{IV} values higher than 1.5 are formed at 10 kbar beneath island arcs, and the amphiboles with Al^{IV} less than 1.5 formed on continental active margins [37]. All the amphiboles of the Sungun dykes have Al^{IV} values less than 1.5 and therefore likely formed in a continental margin setting.

3.8.2 Biotite

The chemical composition of biotite depends on the composition and temperature of the magma, the oxygen fugacity, and the magma's tectonic origin. Using the Al_2O_3 vs MgO and FeO* vs MgO discrimination diagrams (Figure 21), the studied biotite can be classified as having

Table 8: Results of the spot analysis of the epidote of ferromagnesian mineral alteration with its structural formula calculation (LAM)

Sample	FMp2-1	FMp2-2	FMp2-3	FMp2-4	FMp2-5	FMEp3-1	FMEp3-2	FMEp3-3	FMEp3-4	FMEp3-5
SiO_2	37.63	37.38	37.61	37.87	37.61	37.68	36.58	38.03	37.92	37.53
TiO_2	0.00	0.04	0.02	0.05	0.00	0.00	0.00	0.00	0.02	0.02
Al_2O_3	23.30	22.81	23.77	23.13	22.16	21.97	21.60	22.90	23.00	22.05
FeO	12.89	12.68	11.51	12.33	13.46	13.64	13.05	12.76	12.46	13.68
MnO	0.06	0.02	0.05	0.04	0.05	0.05	0.00	0.03	0.06	0.04
MgO	0.00	0.00	0.00	0.05	0.03	0.00	0.04	0.01	0.00	0.00
CaO	22.72	22.82	22.94	22.98	22.89	22.70	21.47	22.94	22.96	22.77
Na_2O	0.00	0.00	0.00	0.00	0.00	0.00	0.00	0.00	0.00	0.00
K2O	0.00	0.00	0.00	0.01	0.00	0.00	0.00	0.00	0.01	0.00
P_2O_5	0.03	0.00	0.04	0.05	0.01	0.02	0.04	0.03	0.04	0.03
Cl	0.00	0.00	0.00	0.00	0.00	0.00	0.00	0.00	0.00	0.00
F	0.00	0.00	0.27	0.02	0.00	0.07	0.10	0.05	0.11	0.22
O=F, Cl	0.00	0.00	−0.12	−0.01	0.00	−0.03	−0.04	−0.02	−0.05	−0.09
Total	96.64	95.76	96.09	96.52	96.20	96.12	92.84	96.73	96.52	96.23
Si	3.10	3.11	3.11	3.12	3.13	3.14	3.15	3.13	3.13	3.13
Ti	0.00	0.00	0.00	0.00	0.00	0.00	0.00	0.00	0.00	0.00
Al	2.26	2.24	2.32	2.24	2.17	2.16	2.19	2.22	2.24	2.17
Fe	0.89	0.88	0.80	0.85	0.94	0.95	0.94	0.88	0.86	0.96
Mn	0.00	0.00	0.00	0.00	0.00	0.00	0.00	0.00	0.00	0.00
Mg	0.00	0.00	0.00	0.01	0.00	0.00	0.01	0.00	0.00	0.00
Ca	2.01	2.03	2.03	2.03	2.04	2.03	1.98	2.02	2.03	2.04
Na	0.00	0.00	0.00	0.00	0.00	0.00	0.00	0.00	0.00	0.00
K	0.00	0.00	0.00	0.00	0.00	0.00	0.00	0.00	0.00	0.00
P	0.00	0.00	0.00	0.00	0.00	0.00	0.00	0.00	0.00	0.00
Cl	0.00	0.00	0.00	0.00	0.00	0.00	0.00	0.00	0.00	0.00
F	0.00	0.00	0.07	0.00	0.00	0.02	0.03	0.01	0.03	0.06
Sum	8.26	8.27	8.26	8.25	8.28	8.30	8.29	8.28	8.29	8.36
P_s	28.18	28.28	25.57	27.45	30.11	30.59	30.00	28.33	27.76	30.57
XFe^{3+}	0.77	0.79	0.72	0.78	0.84	0.86	0.83	0.80	0.78	0.85

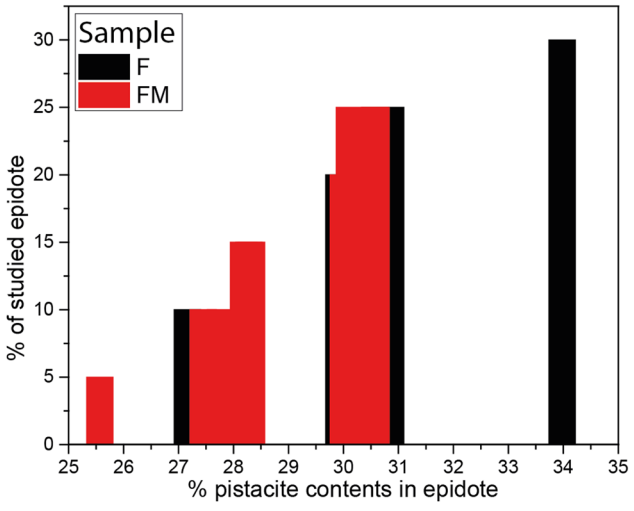

Figure 18: Percentage of pistacite in the epidote of the study area, derived from alteration of plagioclase (F) and ferromagnesian (FM) minerals.

formed in a calc-alkaline orogenic suite (C) [38], and hence, by inference, their host rock was likely formed in an orogenic (continental arc) tectonic environment.

3.9 Geothermobarometry of post-mineralization dykes

3.9.1 Thermobarometry and oxygen fugacity of amphibole

Amphiboles are very useful minerals, because they occur in mafic to felsic rocks and are widely used to calculate the temperature and pressure of crystallization [39–41]. They are broadly accepted as a reliable geothermometer, whereas some uncertainties still surround their accuracy as geobarometer [42–46]. Recently, Ridolfi et al. [47] and Ridolfi and Renzulli [48] have published thermobarometric equations for the estimation of temperature, pressure, oxygen fugacity and dissolved H_2O using amphibole composition changes. Their calibration is valid for amphiboles crystallized from

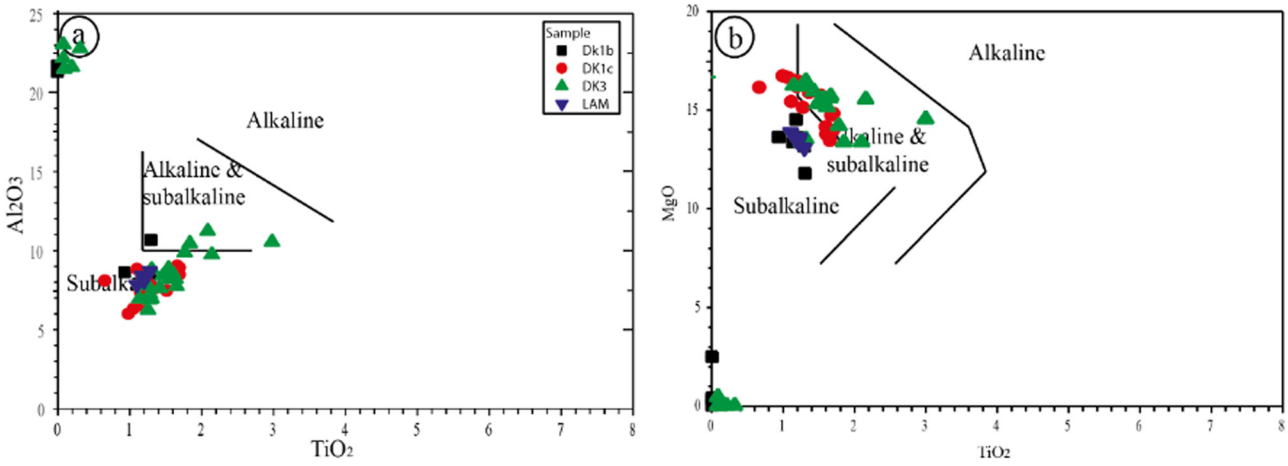

Figure 20: Chemical composition of amphiboles of quartz diorite (DK1b and DK1c), diorite (DK3) and LAM dykes, and associated magmatic suites, after [36]; (a) Al_2O_3 vs. TiO_2; (b) MgO vs. TiO_2.

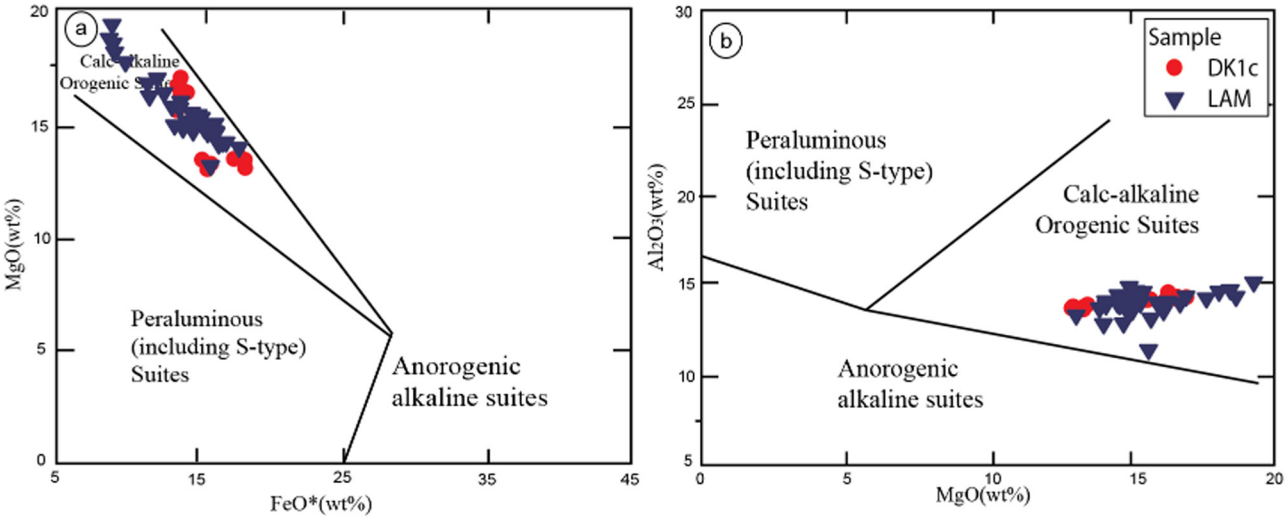

Figure 21: Tectonic discriminant diagrams [38] of (a) MgO vs FeO* and (b) Al_2O_3 vs MgO in biotites of the quartz diorite (DK1c) and LAM dykes.

calc-alkaline and alkaline magmas, and lower to upper crustal pressure, spanning the liquidus to solidus temperature range in intermediate to mafic magma at H_2O saturation to undersaturation. We used their equations to calculate the dependent variables of Si, Ti, Al, Fe, Mg, Ca, Na and K for temperature–pressure estimation. The calculation of temperature and pressure based on the relationships provided by [47] and [48] are summarized in Table 9, and the results are presented in Table 10. As shown in Table 10, the highest calculated temperatures and pressures are 950°C ± 23.5°C and 336 MPa for DK1b and 896°C ± 23.5°C and 231 ± 26 MPa for DK1c. Figure 22 shows the calculated physical and chemical conditions for all the amphibole data in the post-mineralization dykes. In the P–T graph, magnesio-hornblende (DK1b, DK1c and LAM) typically indicates low crystallization pressure (<390 MPa) and temperature (<930°C), low water content and high oxygen fugacity. Oxygen fugacity generally increases from high-temperature and high-pressure magnesio-hastingsite (~nickel-nickel-oxide buffer; NNO −0.3) to low-pressure hornblende (up to NNO +2.5).

Using thermobarometry based on aluminium oxides and titanium in amphibole [49], the crystallization temperatures of the quartz diorite dykes (DK1b, DK1c), diorite (DK3) and LAM were found to be approximately 720, 780, 820 and 800 ± 50°C, respectively, at a pressure of 3–5 kbars (Figure 23).

3.9.2 Biotite

Biotite is a major host of Ti in igneous rocks. Replacement of this element in the biotite structure is

Table 9: Equations used to determine the temperature, pressure and oxygen fugacity [47,48]

Ref.	Variable	Equation
[47]	Temperature	T (°C) = −151.487Si* + 2041; Si* = Si + ($^{[4]}$Al/15) − (2$^{[4]}$Ti) − ($^{[6]}$Al/2) − ($^{[6]}$Ti/1.8) + (Fe^{3+}/9) + (Fe^{2+}/3.3) + (Mg/26) + (^{B}Ca/5) + (^{B}Na/1.3) − (^{A}Na/15) + (^{A}[]/2.3)
	Oxygen fugacity	DNNO = 1.644Mg* − 4.01; Mg* = Mg + (Si/47) − ($^{[6]}$Al/9) − (1.3$^{[6]}$Ti) + (Fe^{3+}/3.7) + (Fe^{2+}/5.2) − (^{B}Ca/20) − (^{A}Na/2.8) + (^{A}[]/9.5)
	Melt H_2O	H_2O melt (wt%) = 5.215$^{[6]}$Al* + 12.28; $^{[6]}$Al* = $^{[6]}$Al + ($^{[4]}$Al/13.9) − ((Si + $^{[6]}$Ti)/5) − ($^{C}Fe^{2+}$/3) − (Mg/1.7) + (^{B}Ca + ^{A}[])/1.2) + (^{A}Na/2.7) − 1.56K − (Fe#/1.6)
	Pressure	P (MPa) = 19.209$e^{(1.438Altot)}$
[48]	Pressure (Eq 1b)	ln P (MPa) = 38.723 − 2.6957*Si − 2.3565*Ti − 1.3006*Al − 2.7780*Fe − 2.4838*Mg − 0.6614*Ca − 0.2705*Na + 0.1117*K
	Pressure (Eq 1c)	P (MPa) = 24,023 − 1,925.3*Si − 1,720.6*Ti − 1,478.5*Al − 1,843.2*Fe − 1,746.9*Mg − 158.28*Ca − 40.444*Na + 253.52*K
	Temperature	T (°C) = 17,098 − 1,322.3*Si − 1,035.1*Ti − 1,208.2*Al − 1,230.4*Fe − 1,152.9*Mg − 130.40*Ca + 200.54*Na + 29.408*K + 24.410*ln P
	Oxygen fugacity	DNNO (log units) = 214.39−17.042*Si−26.080*Ti−16.389*Al−18.397*Fe−15.152*Mg + 0.2162*Ca + 6.1987*Na + 14.389*K
	Melt H_2O	ln H_2O melt (wt%) = −65.907 + 5.0981*Si + 3.1308*Ti + 4.9211*Al + 4.9744*Fe + 4.6536*Mg + 1.0018*Ca − 0.7890*Na − 0.539*K + 0.4642*ln P
	Melt SiO_2	SiO_2 (wt%) = −142.31 + 22.008*Si−15.306*Ti + 2.1880*Al + 16.455*Fe + 12.868*Mg + 0.4085*Ca + 6.7100*Na + 20.980*K − 9.6423*$10^{8}P^{-4}$

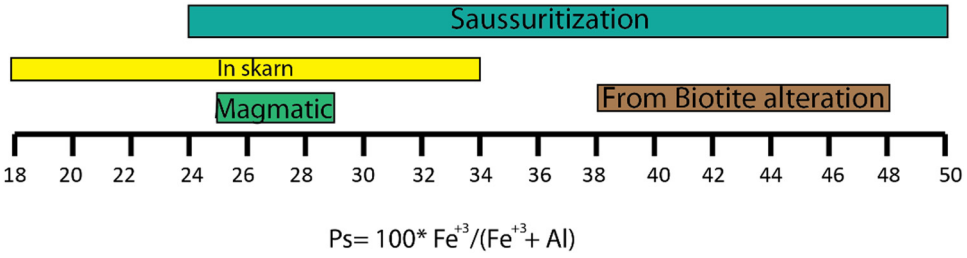

Figure 19: Relationship between pistacite in the types of epidotes and their origin [35]. The studied samples are in the range of saussuritization or resulting from alteration of ferromagnesian minerals.

directly related to the temperature. We use the equation proposed by [50]:

$T = \{[\ln(\mathrm{Ti}) - a - c\,(X_{\mathrm{Mg}})^3]/b\}^{0.333}$, where a, b and c the parameters with values as reported in Table 11. This model is restricted to biotite compositions in the range X_{Mg}; Mg/(Mg + Fe), X_{Mg} = 0.275–1.000, Ti = 0.04–0.60, consistent with the Sungun biotites. Based on this model, the calculated crystallization temperature for the Sungun biotite ranges between 750 and 760°C ± 12°C (Table 12).

3.10 Genetic relationship of post-mineralization dykes with the Sungun porphyry

Field and petrographic investigations of the post-mineralization dykes reveal a wide range of lithologies, including quartz diorite, diorite, gabbrodiorite, MDI, dacite and LAM. The abundance of calcic amphiboles and the presence of biotite and the modelled high fO_2 environment are in agreement with the dykes having been emplaced in the Early Miocene times in an active continental margin, related to subduction of the Neotethys oceanic crust beneath the Central Iranian continent that lasted from the Late Cretaceous to the Neogene. Amphibole thermobarometry using total Al^{3+} content shows that amphibole in the post-mineralization dykes crystalized at 800°C and 4 ± 0.5 kbars. Biotite thermometry gives relatively lower crystallization temperatures of 750 to 760 °C. These indicate the presence of a middle-crustal magmatic storage area in the region. The amphiboles crystallized at about 12 km depth, near the base of the upper continental crust, whereas biotite crystallized at lower temperatures, and presumably at lower pressures, in the upper crust. Thus, pressure calculations based on amphibole indicate pressures in

Table 10: Thermobarometric results and oxygen fugacity for the dykes in R2010 [47] and RR2 012 [48].

	Pressure (MPa)		Temperature		Oxygen fugacity	Melt H_2O		Melt SiO_2	Al#	Species
Sample	RR2012 (Eq 1c)	R2010	RR2012	R2010	R2010	RR2 012	R2010	RR2 012	R2010	R2010
Dk1b	319.16	136.24	944.06	826.09	−12.18	1.33	4.05	80.88	0.12	Mg-Hbl
Dk1b	287.67	151.13	892.93	837.53	−11.82	1.56	4.25	79.00	0.07	Mg-Hbl
Dk1b	274.45	156.54	875.95	834.41	−11.76	1.66	4.55	79.69	0.08	Mg-Hbl
Dk1b	405.27	162.40	984.85	851.13	−11.81	1.31	4.50	77.62	0.12	Mg-Hbl
Dk1b	397.16	158.15	987.32	875.65	−10.77	1.33	3.67	76.91	0.00	Mg-Hbl
Average	336.74	152.89	937.02	844.96	−11.67	1.44	4.20	78.82	0.08	
Min	274.45	136.24	875.95	826.09	−12.18	1.31	3.67	76.91	0.00	
Max	405.27	162.40	987.32	875.65	−10.77	1.66	4.55	80.88	0.12	
DK1c	420.01	161.67	1024.07	868.55	−11.51	1.27	6.35	72.06	0.10	Mg-Hbl
DK1c	421.60	166.78	1023.00	864.36	−11.73	1.27	6.69	72.03	0.13	Mg-Hbl
DK1c	432.98	150.28	1046.50	861.22	−11.67	1.16	6.37	72.97	0.16	Mg-Hbl
DK1c	432.46	157.19	1049.47	861.48	−11.72	1.15	6.47	72.40	0.16	Mg-Hbl
DK1c	317.30	161.71	920.77	857.66	−10.89	1.60	5.23	75.16	0.06	Mg-Hbl
DK1c	209.67	132.69	860.90	833.05	−10.99	1.73	5.09	78.14	0.03	Mg-Hbl
DK1c	58.75	97.51	795.77	801.77	−11.62	1.66	4.44	0.22	0.00	Mg-Hbl
DK1c	105.13	99.82	829.92	805.38	−11.52	1.57	4.42	72.56	0.00	Mg-Hbl
DK1c	87.24	103.14	809.48	806.37	−11.52	1.65	4.47	63.88	0.01	Mg-Hbl
DK1c	98.06	99.58	823.19	798.40	−11.74	1.58	4.44	70.46	0.02	Mg-Hbl
DK1c	72.61	95.91	808.90	808.83	−11.39	1.61	4.44	46.22	0.00	Mg-Hbl
DK1c	222.95	132.65	881.17	831.17	−11.38	1.56	4.70	77.22	0.02	Mg-Hbl
DK1c	154.32	121.57	845.50	823.94	−11.28	1.61	4.57	76.21	0.00	Mg-Hbl
DK1c	292.20	168.78	910.25	855.90	−11.12	1.55	5.13	73.54	0.05	Mg-Hbl
DK1c	335.60	177.62	943.66	867.07	−10.89	1.48	4.89	72.79	0.02	Tsch-Prg
DK1c	150.77	117.04	848.47	819.16	−11.48	1.56	4.59	75.99	0.00	Mg-Hbl
DK1c	123.35	112.76	827.40	820.13	−11.16	1.65	4.42	75.25	0.00	Mg-Hbl
Average	231.47	132.75	896.97	834.38	−11.39	1.51	5.10	67.48	0.04	
Min	58.75	95.91	795.77	798.40	−11.74	1.15	4.42	0.22	0.00	
Max	432.98	177.62	1049.47	868.55	−10.89	1.73	6.69	78.14	0.16	
DK3	416.28	168.95	977.81	857.13	−11.68	1.39	4.93	76.64	0.15	Mg-Hbl
DK3	592.21	204.31	1170.61	905.13	−10.40	0.77	3.62	69.61	0.04	Mg-Hst
DK3	689.30	255.86	1216.50	939.11	−10.34	0.65	3.40	64.95	0.03	Mg-Hst
DK3	73.62	104.08	814.01	820.25	−11.09	1.61	4.26	47.15	0.00	Mg-Hbl
DK3	130.04	112.20	849.18	816.99	−11.28	1.54	4.33	75.68	0.00	Mg-Hbl
DK3	106.86	105.75	832.60	821.46	−11.03	1.59	4.41	72.58	0.00	Mg-Hbl
DK3	275.51	153.68	921.16	852.23	−10.91	1.48	4.56	74.84	0.01	Mg-Hbl
DK3	208.67	129.59	896.22	836.87	−11.14	1.44	4.19	75.75	0.00	Mg-Hbl
DK3	573.91	314.21	1057.95	926.60	−10.40	1.38	5.53	65.93	0.08	Tsch-Prg
DK3	520.90	262.56	1037.98	905.50	−10.70	1.37	5.56	68.46	0.08	Tsch-Prg
DK3	464.12	223.72	1021.58	893.23	−10.63	1.34	5.04	70.09	0.05	Tsch-Prg
DK3	296.76	167.27	926.04	857.36	−10.90	1.50	4.87	73.94	0.04	Mg-Hbl
DK3	241.25	143.06	910.28	843.65	−11.03	1.46	4.43	75.25	0.00	Mg-Hbl
DK3	271.16	155.42	922.90	848.64	−11.09	1.45	4.70	74.60	0.03	Mg-Hbl
DK3	89.41	104.14	827.06	825.85	−10.91	1.57	4.29	64.71	0.00	Mg-Hbl
DK3	174.18	124.29	873.50	834.42	−10.99	1.51	4.37	76.45	0.00	Mg-Hbl
DK3	264.47	144.05	925.49	851.69	−10.90	1.41	4.32	74.87	0.00	Mg-Hbl
Average	316.98	169.01	951.82	860.95	−10.91	1.38	4.52	70.68	0.03	
Min	73.62	104.08	814.01	816.99	−11.68	0.65	3.40	47.15	0.00	
Max	689.30	314.21	1216.50	939.11	−10.34	1.61	5.56	76.64	0.15	
LAM	253.32	135.26	886.61	826.86	−11.85	1.54	4.36	79.80	0.08	Mg-Hbl
LAM	307.63	144.93	925.51	834.70	−11.88	1.42	4.18	79.28	0.07	Mg-Hbl
LAM	385.84	171.64	968.35	858.57	−11.55	1.39	4.29	76.82	0.06	Mg-Hbl

Table 10: continued

	Pressure (MPa)		Temperature		Oxygen fugacity	Melt H_2O		Melt SiO_2	Al#	Species
Sample	**RR2012 (Eq 1c)**	**R2010**	**RR2012**	**R2010**	**R2010**	**RR2 012**	**R2010**	**RR2 012**	**R2010**	**R2010**
LAM	315.21	150.14	929.92	841.08	−11.69	1.44	4.20	78.49	0.06	Mg-Hbl
LAM	338.68	156.89	941.49	843.24	−11.72	1.42	4.19	78.67	0.09	Mg-Hbl
Average	320.14	151.77	930.38	840.89	−11.74	1.44	4.24	78.61	0.07	
Min	253.32	135.26	886.61	826.86	−11.88	1.39	4.18	76.82	0.06	
Max	385.84	171.64	968.35	858.57	−11.55	1.54	4.36	79.80	0.09	

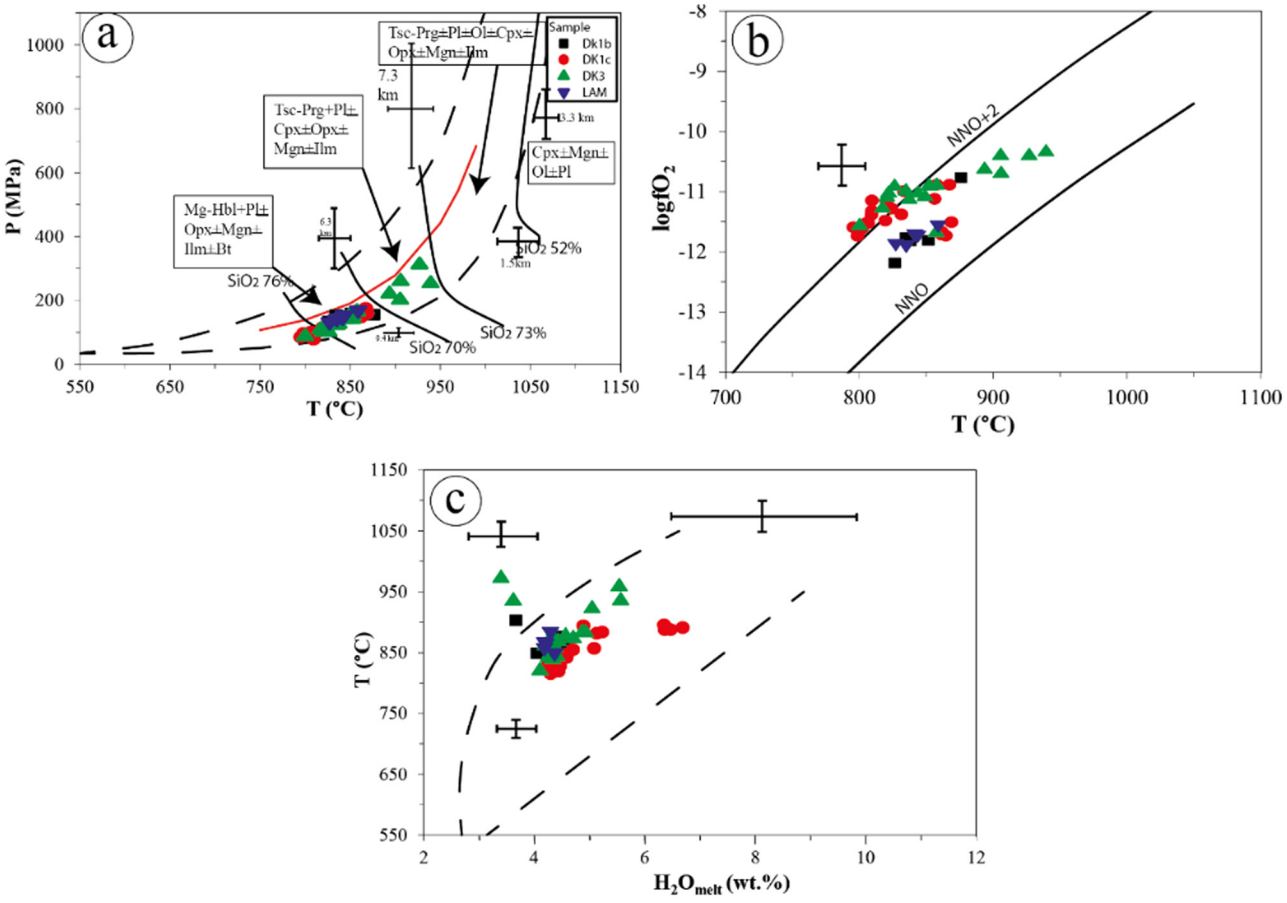

Figure 22: Conditions of pressure and temperature crystallization of amphibole determined by thermobarometry: (a) T–P chart, (b) T–logfO_2 graph and (c) H_2O–T chart [47,48].

the deep storage area, not in the shallower upper crust, where the Sungun porphyry Cu–Mo deposit formed. Subsequently, the dykes solidified at lower temperatures and pressures. According to Ti-in-zircon thermometry, the mineralized Sungun porphyry stock and the post-mineralization dykes were crystalized at about 650 and 700°C, respectively [12]. Rare earth element abundances in the zircon crystals additionally show that the Sungun porphyry crystallized from a high fO_2 melt [12]. These petrological and tectonic analogies suggest a relationship of the post-mineralization dykes with the magmatic system that generated the Sungun porphyry and the related Cu–Mo mineralization. Dykes may represent residual melts that were reactivated after the mineralizing event and intruded the deposit. The whole-rock geochemical studies [51] support this interpretation. Both rock suites have similarities in their rare earth element patterns as well as strontium and neodymium

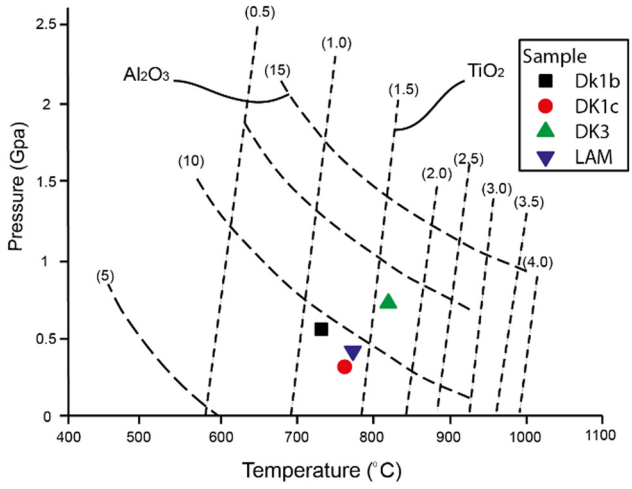

Figure 23: Isopleths of Al_2O_3 and TiO_2 in amphiboles based on weight percentage for determining the pressure and temperature of the post-mineralization quartz diorite (DK1b, DK1c), diorite (DK3) and LAM dykes [49].

Table 11: The fixed values used in geothermometry based on the amount of Ti in biotite

Coefficient	Value	Standard error	95% confidence limits
a	−2.3594	0.0141	−2.3870 to −2.3317
b	4.6482 $\times 10^{-9}$	5.1970 $\times 10^{-11}$	4.5461 $\times 10^{-9}$ to 4.7503 $\times 10^{-9}$
c	−1.7283	0.0584	−1.8432 to −1.6134

Table 12: Data from biotite geothermometry in the quartz diorite (DK1c) and LAM dykes

Sample	T (°C)	Sample	T (°C)	Sample	T (°C)
DK1c	768.61	Max	777.77	LAM	789.86
DK1c	775.49	Min	733.62	LAM	770.89
DK1c	776.93	Average	756.61	LAM	773.09
DK1c	777.77	LAM	754.97	LAM	742.61
DK1c	773.73	LAM	784.96	LAM	732
DK1c	775.74	LAM	774.48	LAM	718.54
DK1c	773.76	LAM	784.56	LAM	743.6
DK1c	752.96	LAM	784.23	LAM	720.57
DK1c	773.12	LAM	790.26	LAM	752.21
DK1c	771.94	LAM	789.71	LAM	738.41
DK1c	735.5	LAM	785.07	LAM	725.58
DK1c	735.65	LAM	785.56	LAM	750.22
DK1c	733.62	LAM	785.97	LAM	733.87
DK1c	736.74	LAM	772.21	Max	790.26
DK1c	737.64	LAM	768.5	Min	718.54
DK1c	745.18	LAM	764.43	Average	762.58
DK1c	740.32	LAM	782.89		
DK1c	736.1	LAM	769.43		

isotopes, which indicates a common source and evolutionary processes. The Sungun porphyry stock is therefore the oldest and most felsic member of the magmatic complex [51], with later intrusions tapping more primitive and potentially recharged portions of it to form quartz diorite, diorite and gabbrodiorite.

4 Conclusion

The compositions of the post-mineralization dykes intruding the Sungun copper–molybdenum porphyry are quartz diorite, diorite, gabbrodiorite, dacite, MDI and LAM. The main modal minerals of these dykes are plagioclase, amphibole and biotite. Mineral chemistry indicates that plagioclase compositions range from labradorite to albite, amphibole has magnesio-hornblende composition and biotite is primary magmatic magnesium-biotite to phlogopite. Secondary chlorite is pycnochlorite. The presence of epidote in these rocks may indicate injection of calcium-rich solutions into them in different phases of alteration. According to texture and percentage of pistacite, epidotes formed through alteration processes. Geothermometers indicate crystallization temperatures of 951 to 896°C based on amphibole compositions and 760 to 750°C based on biotite. Amphibole barometry results in crystallization pressure of about 380 MPa, equivalent to a depth of 12 km. Oxygen barometers, applied to both amphiboles and biotite in the Sungun dykes, indicate high oxygen fugacity, suggesting magmatic oxidizing conditions (above that of the NNO buffer) during crystallization. The chemical composition of mineral phases in the post-mineralization dykes intruding the Sungun porphyry indicates that they are formed from a calc-alkaline to alkaline magmatic suite emplaced in a continental arc setting.

References

[1] Babakhani ARLJL, Rico R. Geological quadranglemap of Ahar, Geological Survey of Iran. 1990;1:250000

[2] Castro A, Aghazadeh M, Badrzadeh Z, Chichorro M. Late eocene–oligocene post-collisional monzonitic intrusions from the Alborz magmatic belt, NW Iran. An example of monzonite magma generation from a metasomatized mantle source. Lithos. 2013;180:109–27.

[3] Shafiei B, Shahabpour J. Geochemical aspects of molybdenum and precious metals distribution in the Sar Cheshmeh

porphyry copper deposit, Iran. Miner Deposita. 2011;47:535–43.
[4] Calagari AA. Geochemical, Stable Isotope, Noble Gas and Fluid Inclusion Studies of Mineralization and Alteration at Sungun Porphyry Copper Deposit, East Azarbaidjan, Iran: Implications for Genesis. 1997, University of Manchester.
[5] Hezarkhani A. Petrology of the intrusive rocks within the Sungun porphyry copper deposit, Azerbaijan, Iran. J Asian Earth Sci. 2006;27(3):326–40.
[6] Alavi G. Study of the skarn deposits around the Sheyvar-Dagh batolith and comparison with the Sungun porphyry skarn, in Geology. Tabriz. 2014
[7] Izadyar J. The study of petrography and petrology of igneous rocks Sungun deposit area. Shahid Beheshti. 1995
[8] Jamali H, Dilek Y, Daliran F, Yaghubpur A, Behzad M. Metallogeny and tectonic evolution of the Cenozoic Ahar–Arasbaran volcanic belt, northern Iran. Int Geol Rev. 2010;52(4–6):608–30.
[9] Mehrpartou M. Contributions to the geology, geochemistry, ore genesis and fluid inclusion investigations on Sungun Cu–Mo porphyry deposit (North-West of Iran). 1993.
[10] Hassanpour S. Metallogeny and Mineralization of Copper and Gold in Arasbaran Zone (Eastern Azerbaijan) in Geology. Shahid Beheshti. 2010, p. 310.
[11] Moayyed M. Petrographic and Mineralographic report of Sungun copper deposit, 1, Editor. 2004.
[12] Aghazadeh M, Hou Z, Badrzadeh Z, Zhou L. Temporal–spatial distribution and tectonic setting of porphyry copper deposits in Iran: constraints from zircon U–Pb and molybdenite Re–Os geochronology. Ore Geol Rev. 2015;70:385–406.
[13] Kamali A. Petrology and mineral chemistry of post mineralization dykes of SUNGUN Cu–Mo porphyry deposit, North of Varzegan, East Azerbaijan. PhD thesis, Tabriz, Iran: University of Tabriz; 2016.
[14] Stocklin J. Structural history and tectonics of Iran: a review. AAPG Bull. 1968;52(7):1229–58.
[15] Nabavi M. An introduction to the geology of Iran, Geological Survey of Iran, Farsi. 1976.
[16] Nezafati N. Au–Sn–W–Cu-Mineralization in the Astaneh-Sarband Area, West Central Iran including a comparison of the ores with ancient bronze artifacts from Western Asia. PhD thesis, University of Freiberg; 2006.
[17] Kamali A, Moayyed M, Amel N, Hosseinzadeh M. Mineral chemistry and geochemistry of lamprophyric dykes in the Sungun Cu–Mo porphyry deposit (Varzaghan–Northwestern Iran). Geosci Sci Q J. 2017;26:73–90.
[18] Kamali A, Mohsen M, Amel N, Hosainzadeh M. Mineralogy and mineral chemistry of quartz-dioritic dykes of Sungun Mo–Cu porphyry deposit (NW Iran). Iran. J Crystallogr Miner. 2017;25:123–38.
[19] Deer WA, Howie RA, Zussman J. An introduction to the rock-forming minerals. Hong Kong: Longman Scientific & Technical; 1992, vol. 2
[20] Leake BE, Woolley AR, Arps CES, Birch WD, Charles Gilbert M, Grice JD, et al. Report. Nomenclature of amphiboles: report of the subcommittee on amphiboles of the international mineralogical association commission on new minerals and mineral names. Mineral Mag. 1997;1(2):295–321.
[21] Jarrar G. Mineral chemistry in dioritic hornblendites from Wadi Araba, southwest Jordan. J Afr Earth Sci. 1998;26(2):285–95.
[22] Kharbish S. Geochemistry and magmatic setting of Wadi El-Markh island-arc gabbro–diorite suite, central Eastern Desert, Egypt. Chem Erde-Geochem. 2010;70(3):257–66.
[23] Coulson I. Evolution of the North Qôroq centre nepheline syenites, South Greenland: alkali-mafic silicates and the role of metasomatism. Mineral Mag. 2003;67(5):873–92.
[24] Rieder M, Cavazzini G, D'yakonov YS, Frank-Kamenetskii VA, Gottardi G, Guggenheim S, et al. Nomenclature of the micas. Clays Clay Miner. 1998;46(5):586–95.
[25] Dymek RF. Titanium, aluminum and interlayer cation substitutions in biotite from high-grade gneisses' West Greenland. Am Mineral. 1983;6:880–99.
[26] Nachit H, Ibhi A, Abia EH, Ohoud MB. Discrimination between primary magmatic biotites, reequilibrated biotites and neoformed biotites. C R Geosci. 2005;337(16):1415–20.
[27] Miller CF, Stoddard EF. The role of manganese in the paragenesis of magmatic garnet: an example from the Old Woman-Piute Range, California. J Geol. 1981;89(2):233–46.
[28] Zen EA. Phase relations of peraluminous granitic rocks and their petrogenetic implications. Annu Rev Earth Planet Sci. 1988;16(1):21–51.
[29] Hey MH. A new review of the chlorites. Mineral Mag. 1954;30:277–92.
[30] Franz G, Liebscher A. Physical and chemical properties of the epidote minerals–an introduction. Rev Mineral Geochem. 2004;56(1):1–81.
[31] Plissart G, Féménias O, Mărunțiu M, Diot H, Demaiffe D. Mineralogy and geothermometry of gabbro-derived listvenites in the Tisovita–Iuti ophiolite, Southwestern Romania. Can Mineral. 2009;47(1):81–105.
[32] Zen EA, Hammarstrom JM. Magmatic epidote and its petrologic significance. Geology. 1984;12(9):515–8.
[33] Holdaway MJ. Thermal stability of Al–Fe epidote as a function of and Fe content. Contrib Mineral Petrol. 1972;37(4):307–40.
[34] Armbruster T, Bonazzi P, Akasaka M, Bermanec V, Chopin C, Gieré R, et al. Recommended nomenclature of epidote-group minerals. Eur J Mineral. 2006;18(5):551–67.
[35] Mazaheri A. The importance of pistacite in the diagnosis of epidote. The 8th Seminar of Crystallography and Mineralogy of Iran. Tehran: University of Science and Technology; 1999
[36] Molina JF, Scarrow JH, Montero PG, Bea F. High-Ti amphibole as a petrogenetic indicator of magma chemistry: evidence for mildly alkalic-hybrid melts during evolution of Variscan basic–ultrabasic magmatism of Central Iberia. Contrib Mineral Petrol. 2009;158(1):69–98.
[37] Ghent E, Nicholls J, Simony PS, Sevigny JH, Stout MZ. Hornblende geobarometry of the Nelson Batholith, south-eastern British Columbia: tectonic implications. Can J Earth Sci. 1991;28(12):1982–91.
[38] Abdel-Rahman AFM. Nature of biotites from alkaline, calc-alkaline, and peraluminous magmas. J Petrol. 1994;35(2):525–41.
[39] Arculus RJ, Wills KJ. The petrology of plutonic blocks and inclusions from the Lesser Antilles island arc. J Petrol. 1980;21(4):743–99.
[40] Cawthorn RG, Curran E, Arculus R. A petrogenetic model for the origin of the calc-alkaline suite of Grenada, Lesser Antilles. J Petrol. 1973;14(2):327–37.
[41] Davidson J, Turner S, Handley H. Amphibole "sponge" in arc crust? Geology. 2007;35(9):787–90.

[42] Bachmann O, Dungan MA. Temperature-induced Al-zoning in hornblendes of the Fish Canyon magma, Colorado. Am Mineral. 2002;87(8–9):1062–76.
[43] Barnes CG. Mineralogy of the Wooley Creek batholith, Slinkard pluton, and related dikes, Klamath Mountains, northern California. Am Mineral. 1987:72(9–10):879–901.
[44] Blundy JD, Holland TJ. Calcic amphibole equilibria and a new amphibole-plagioclase geothermometer. Contrib Mineral Petrol. 1990;104(2):208–24.
[45] Rutherford MJ, Devine JD. Magmatic conditions and magma ascent as indicated by hornblende phase equilibria and reactions in the 1995–2002 Soufriere Hills magma. J Petrol. 2003;44(8):1433–53.
[46] Shane P, Smith VC. Using amphibole crystals to reconstruct magma storage temperatures and pressures for the post-caldera collapse volcanism at Okataina volcano. Lithos. 2013;156:159–70.
[47] Ridolfi F, Renzulli A, Puerini M. Stability and chemical equilibrium of amphibole in calc-alkaline magmas: an overview, new thermobarometric formulations and application to subduction-related volcanoes. Contrib Mineral Petrol. 2010;160(1):45–66.
[48] Ridolfi F, Renzulli A. Calcic amphiboles in calc-alkaline and alkaline magmas: thermobarometric and chemometric empirical equations valid up to 1,130°C and 2.2 GPa. Contrib Mineral Petrol. 2012;163(5):877–95.
[49] Ernst W, Liu J. Experimental phase-equilibrium study of Al- and Ti-contents of calcic amphibole in MORB–a semiquantitative thermobarometer. Am Mineral. 1998;83(9–10): 952–69.
[50] Henry DJ, Guidotti CV, Thomson JA. The Ti-saturation surface for low-to-medium pressure metapelitic biotites: implications for geothermometry and Ti-substitution mechanisms. Am Mineral. 2005; 90(2–3):316–28.
[51] Kamali AA, Moayyed M, Amel N, Hosseinzadeh MR, Mohammadiha K, Santos JF, et al. Post-mineralization, cogenetic magmatism at the sungun Cu–Mo porphyry deposit (Northwest Iran): protracted melting and extraction in an arc system. Minerals. 2018;8(12):588.